




# Fused exosomal targeted therapy in periprosthetic osteolysis through regulation of bone metabolic homeostasis

Tianliang Ma<sup>1</sup>, Qimeng Liu<sup>1</sup>, Zheyu Zhang, Jiangyu Nan, Guanzhi Liu, Yute Yang, Yihe Hu<sup>\*</sup>, Jie Xie<sup>\*\*</sup> 

Department of Orthopedics, The First Affiliated Hospital, Zhejiang University School of Medicine, No.79 Qingchun Road, Hangzhou, Zhejiang, 310003, China

## ARTICLE INFO

### Keywords:

Fused exosome  
M2 macrophage-derived exosomes  
Urine-derived stem cell exosomes  
Periprosthetic osteolysis  
Bone metabolic homeostasis

## ABSTRACT

The onset of periprosthetic osteolysis is mediated by wear particles following artificial arthroplasty. This manifests as a disturbed bone metabolism microenvironment, characterized by insufficient osteogenesis and angiogenesis, and enhanced osteoclastic activity. To target and remodel the homeostatic environment of bone metabolism in the sterile region around the prosthesis, we successfully pioneered the proposal and construction of a fused exosome (f-exo) system with M2 macrophage-derived exosomes (M2-exo) and urine-derived stem cell exosomes (USC-exo). The results demonstrate that f-exo effectively combines the osteolysis region-targeting capabilities of M2-exo with the bone metabolic homeostasis modulation effects of two exosomes (M2-exo and USC-exo), thereby achieving a significantly enhanced bone metabolic homeostasis targeting effect in the periprosthetic osteolysis region. The proteomic analysis of M2-exo, USC-exo, and f-exo revealed the potential mechanism of f-exo in targeting-regulation of bone metabolic homeostasis. Our study employs an innovative approach utilizing the fused exosome system for exosome targeted delivery, which offers a novel intervention strategy for the clinical management of periprosthetic osteolysis. Furthermore, it provides a novel conceptual framework for the development of exosome-based drug-targeting delivery systems.

## 1. Introduction

Artificial joint replacement is the surgical procedure by which a diseased joint is replaced with an artificial joint. It is a treatment option for patients who have lost the normal joint structure and function due to joint degeneration, inflammatory arthropathy, or trauma, among other causes. Artificial joint replacement is the preferred method and ultimate treatment for end-stage joint diseases. The objective of artificial joint replacement surgery is to treat joint diseases, relieve joint pain, and reconstruct joint function. It is the preferred method and ultimate treatment for end-stage joint diseases. A review reveals that the rate of revision following initial joint replacement surgery is approximately 4–6 % after 10 years [1], and the rate of revision within 15 years is approximately 10 % per million total hip replacements [2]. The most common cause of revision surgery after total joint replacement is

non-infectious loosening of the joint prosthesis at the interface with the bone, i.e., aseptic loosening of the prosthesis, with an incidence of about 10 % at 10 years after surgery, accounting for more than 30 % of all revision surgeries [1,3]. The current non-surgical treatments for aseptic loosening of prostheses are ineffective, and revision surgery is costly [4]. Therefore, there is an urgent need to further define the pathogenesis of aseptic loosening of prostheses and to explore clinical prevention and treatment strategies. The precise mechanism underlying the aseptic loosening of the prosthesis remains elusive. However, extant studies indicate that periprosthetic osteolysis driven by wear particles represents a pivotal factor in the pathogenesis of aseptic loosening of the prosthesis [5]. The release of wear particles from prosthetic components or articular surfaces induced by exercise over time creates a localized aseptic inflammatory environment. This environment promotes the recruitment of immune cells, the development of chronic granulomatous

Peer review under the responsibility of editorial board of Bioactive Materials.

\* Corresponding author.

\*\* Corresponding author.

E-mail addresses: [tianliangma@163.com](mailto:tianliangma@163.com) (T. Ma), [liuqm\\_med@163.com](mailto:liuqm_med@163.com) (Q. Liu), [3180102491@zju.edu.cn](mailto:3180102491@zju.edu.cn) (Z. Zhang), [12318682@zju.edu.cn](mailto:12318682@zju.edu.cn) (J. Nan), [liuguanzhi1029@stu.xjtu.edu.cn](mailto:liuguanzhi1029@stu.xjtu.edu.cn) (G. Liu), [yyyyyt@zju.edu.cn](mailto:yyyyyt@zju.edu.cn) (Y. Yang), [xy\\_huyh@163.com](mailto:xy_huyh@163.com) (Y. Hu), [dr\\_xiejie@zju.edu.cn](mailto:dr_xiejie@zju.edu.cn) (J. Xie).

<sup>1</sup> These authors contributed equally to this work.

<https://doi.org/10.1016/j.bioactmat.2025.04.006>

Received 4 November 2024; Received in revised form 18 March 2025; Accepted 3 April 2025

Available online 8 April 2025

2452-199X/© 2025 The Authors. Publishing services by Elsevier B.V. on behalf of KeAi Communications Co. Ltd. This is an open access article under the CC BY-NC-ND license (<http://creativecommons.org/licenses/by-nc-nd/4.0/>).

inflammation, and the generation of pathologic periprosthetic membranes [6]. In essence, an environment characterized by chronic inflammation, which is mediated by periprosthetic wear particles, results in an imbalance in bone metabolic homeostasis. This, in turn, gives rise to progressive periprosthetic osteolysis and aseptic loosening.

The homeostatic regulation of bone metabolism is a highly coordinated and dynamic process whereby bone production replaces aged or damaged bone, which is essential for maintaining bone health [7,8]. The maintenance of the structural and functional integrity of a healthy skeleton is contingent upon the processes of bone remodeling within the context of homeostatic bone metabolism. The coupled effects of osteogenesis, bone resorption, and angiogenesis collectively contribute to the maintenance of the body's bone metabolic homeostasis [9]. An adequate blood supply to the site of bone remodeling is conducive to the input of raw materials and nutrients for bone metabolism and the output of metabolites, which facilitates the coupling of bone production and bone resorption in a physiological state [10]. A sophisticated and well-organized communication system exists between endothelial cells, osteoblasts, and osteoclasts, which collaborate to maintain bone homeostasis through various modes of crosstalk. Endothelial cells migrate and proliferate to form new blood vessels, which serve as a scaffold for osteoblasts and osteoclasts [11], and osteoclasts secrete platelet-derived growth factor-BB to induce endothelial cell angiogenesis during bone remodeling and to support bone marrow-derived mesenchymal stem cell differentiation into osteoblasts. The primary mode of communication between osteoblasts and osteoclasts is through intercellular contacts and diffusible paracrine factors [12]. On the one hand, osteoblasts and osteoclasts form gap junctions, which facilitate the exchange of material and information [13]; on the other hand, osteoblasts release the regulators of osteoclast survival and differentiation, M-CSF, RANKL, and OPG, which regulate survival, differentiation, cell migration, and activation of osteoclasts and macrophages. Additionally, OPG inhibits osteoclast recruitment and activation by binding to RANKL [14,15]. An imbalance of bone metabolic homeostasis around the periprosthetic area following arthroplasty can result in the development and progression of periprosthetic osteolysis. The primary mechanisms underlying this phenomenon are decreased angiogenesis and osteogenesis, coupled with increased bone resorption. The promotion of angiogenesis and osteogenesis, coupled with the inhibition of bone resorption, represent a promising strategy for combating periprosthetic osteolysis. Nevertheless, there is a paucity of comprehensive research elucidating the precise regulatory mechanisms governing the wear particle-induced imbalance of periprosthetic bone metabolism in periprosthetic osteolysis.

Urine-derived stem cells (USC) are derived from fresh human urine and possess several advantageous characteristics, including ease of collection, non-invasive access, sustainable production, and minimal ethical concerns [16]. It has been demonstrated that urine-derived stem cell exosomes (USC-exo) exert a pivotal influence on the regulation of bone metabolic homeostasis through the enrichment of microRNAs and proteins. USC-exo has been demonstrated to facilitate the repair of osteonecrosis [17], hindlimb ischemia, and diabetic wounds by stimulating angiogenesis [18,19]. Additionally, it has been shown to play a role in the treatment of osteoporosis by promoting osteogenesis and inhibiting bone resorption [20]. The aforementioned evidence demonstrates that USC-exo exhibits considerable promise for clinical utilization in the domain of bone tissue regeneration. Moreover, the prospective application of USC-exo for the prevention and management of periprosthetic osteolysis is encouraging. Nevertheless, the *in vivo* release of USC-exo is not stable and lacks the capacity to be delivered in a targeted manner to the periprosthetic area. Consequently, there is a necessity to synthesize a stable USC-exo delivery system with osteolysis-targeting properties [21]. Exosomes represent an optimal vehicle for drug delivery. Their phospholipid bilayer structure provides a foundation for drug-delivery liposomes [22]. Furthermore, exosome drug carriers exhibit tissue-specificity, stability, and an internalization pathway analogous to that of liposomes, which enables the targeted

delivery of drugs. It is of significant importance to note that exosomes inherit the surface components and regulatory molecules of the parental cells, thereby acquiring the biological properties of the parental cells [23]. M2 macrophage-derived exosomes (M2-exo) exhibit the same properties as their parental macrophages, including the ability to home to sites of inflammation, migrate in response to inflammatory chemotaxis, and evade immune responses. These functions are closely associated with the membrane surface molecules selectin, glycoprotein ligands, and RGD integrins [24]. Furthermore, evidence indicates that M2-exo has the biological function of promoting angiogenesis and osteogenesis while inhibiting bone resorption [25–27]. In conclusion, we propose the investigation of the feasibility of developing an M2-exo-USC-exo delivery system to achieve the synergistic effect of regional targeting of osteolysis and homeostatic regulation of bone metabolism.

The construction of membrane fusion-based drug-targeted delivery systems represents an effective means to achieve specific functions. Existing studies have focused on the fusion of cell membranes, cell membrane-encapsulated exosomes, and exosomal liposome fusion. The fusion of tumor cell membranes with mitochondrial membranes endows nanoparticles with the capacity to traverse the blood-brain barrier and target mitochondria of glioma cells, thereby enhancing the biocompatibility and blood circulation time of biomimetic nanomedicine systems [28]. The utilization of platelet membrane-coated mesenchymal stem cell exosomes has been demonstrated to enhance the efficiency of exosome delivery at atherosclerotic plaques, thereby augmenting the efficacy of the treatment regimen [29]. ROS-responsive exosome-liposome hybrid nanovesicles have been developed to deliver anti-Alzheimer's disease siRNAs synergistically. This is achieved by utilizing the homing ability of exosomes and the nucleic acid-loading ability of liposomes, which effectively enhances the accumulation of drugs at the lesion site [30]. The structural basis for the aforementioned drug delivery systems is phospholipid bilayers, which collectively facilitate biological functions such as targeted delivery, immune evasion, prolonged circulation, and are deemed safe for *in vivo* application. In light of the aforementioned theoretical and technical foundations and the distinctive carrier attributes of M2-exo, we put forth a proposal to achieve the targeted delivery of exosome through the natural targeting of M2-exos to areas of osteolysis region. This will be accomplished through exosome fusion, with the two exosomes in the region of osteolysis functioning synergistically to regulate bone metabolism. The fused exosome is anticipated to serve as a precise and reliable targeted molecular drug for the prevention and treatment of periprosthetic osteolysis.

## 2. Materials and methods

### 2.1. Materials

DMEM medium (CYTOCH, Shanghai, China), RPMI 1640 medium (BioChannel Biological Technology Co., Ltd.); Fetal Bovine serum (Gibco, USA); Exosome-depleted Fetal Bovine serum (Umibio (Shanghai) Co., Ltd.); Penicillin-Streptomycin Liquid (BDBIO HangZhou China); Cell Freezing Medium (A401; Witcel, Shanghai, China); Trypsin (HAKATA); PBS, TBST (ABclonal Technology, WuHan, China); Cell Plasma Membrane Staining Kit with DiI, DiO, Reactive Oxygen Species assay kit, 4 %PFA, Alkaline Phosphatase Stain Kit (Beyotime, China); Complete Medium For BMSC Culture Osteogenic Differentiation (Ori-Cell®, from Cyagen Biosciences (Guangzhou) Inc.); Goat Serum Albumin (Biodragon, AbBox, China); TRAP Activity Assay, Kit Modified Sirius Red Stain Kit (Beijing Solarbio Science & Technology Co., Ltd.); FITC Phalloidin, DiI Iodide (Yeasen Biotechnology (Shanghai) Co., Ltd.); BCA Protein Quantification Kit (Smar-lifesciences, SLR01201); SDS-PAGE Loading Buffer (Swiss Affinibody LifeScience AG); Titanium nanopowder (Aladdin, Shanghai); Anti-GAPDH antibody (Abcam, UK), Anti-CD63 antibody (Abcam, UK), Anti-TSG101 antibody (Abcam, UK), Anti-Calnexin antibody (Abcam, UK), Anti-coll1a antibody (Abcam, UK),

Anti-sp7 antibody (Abcam, UK), Anti-runx2 antibody (Abcam, UK), Anti-CTSK antibody (Abcam, UK), Anti-NFATc-1 antibody (Abcam, UK), Anti-TRAP antibody (Abcam, UK), Anti-EMCN antibody (Proteintech, China), Anti-HIF1 $\alpha$  antibody (Abcam, UK), Anti-CD31 antibody (Abcam, UK), Anti-VEGF antibody (Abcam, UK). Western Quick Block Kit (GenScript Corporation, China); NCM Universal Antibody Diluent (New Cell & Molecular Biotech); Total RNA Extraction Kit (ACCURATE BIOTECHNOLOGY(HUNAN) CO., LTD, Changsha, China); HotStart 2X SYBR Green qPCR Master Mix (APEXbio, USA); Transwell system (NEST Biotechnology, China); Corning® Matrigel® (Corning, USA), confocal culture dish (SAINING Biotechnology).

## 2.2. Study approval

The collection of urine samples and their use for scientific research was approved by Clinical Research Ethics Committee of the First Affiliated Hospital of Zhejiang University School of Medicine (No. 11T20230385B-R1). Animal experimentation procedures adhered strictly to protocols approved by the Experimental Animal Ethics Committee of the First Affiliated Hospital of Zhejiang University School of Medicine (2023 No. 1394), and all experimental animals were kept under SPF conditions during the experiments.

## 2.3. Cell lines and conditions

Human USC: isolation of human USC, culture, and extraction of USC-exo are described in detail in our previous study [31].

Human bone marrow-derived macrophages (BMDM) and M2 polarization induction: We used previously reported methods to isolate bone marrow mononuclear cells [32], and RPMI 1640 medium (BioChannel Biological Technology Co., Ltd.) containing M-CSF (20 ng/mL) was used to induce BMDM maturation, then IL-4 (20 ng/mL) & IL-13 (10 ng/mL) was applied to induce M2 polarization. Flow cytometry was used to characterize the altered CD206 expression after BMDM induction.

RAW264.7 cells: The RAW264.7 cell line was obtained from the American Type Culture Collection (ATCC, Manassas, VA, USA) and cultured in DMEM medium with 10 % FBS (UmediumHeFei China).

Mouse Bone marrow-derived mesenchymal stem cells (BMSC): BMSC were isolated using previously reported methods, and BMSC were cultured in the DMEM complete medium [33].

HUVEC: HUVEC cell lines were obtained from the American Type Culture Collection (ATCC, Manassas, VA, USA) and cultured in complete DMEM with 10 % FBS (Inner Mongolia Opcel Biotechnology Co., Ltd).

## 2.4. Flow cytometry identification of M2 macrophage and USC

Cells were harvested and stained with antibodies specific to the M2 macrophage marker (CD68 CD206) and USC markers (CD34, CD45, CD73, CD90), cells were incubated with the respective primary antibodies for 30 min at 4 °C, followed by incubation with appropriate fluorochrome-conjugated secondary antibodies. The cells were analyzed using a flow cytometry (Challenbio, China), and data were processed with FlowJo software.

## 2.5. Exosome isolation

We used differential centrifugation to collect exosomes, and all steps of exosome isolation were performed at 4 °C. Exosome-free complete medium was used to culture M2 macrophages and USC. After reaching a confluence of 80 %, the conditioned medium was collected and filtered through a 0.22  $\mu$ m filter (Guangzhou Jet Bio-Filtration Co., Ltd.) to remove cells and debris. Exosomes were isolated using differential ultracentrifugation. Briefly, the conditioned medium was first centrifuged at 500 $\times$ g for 10 min to remove dead cells, followed by a 2000 $\times$ g spin for 20 min to eliminate larger debris. The supernatant was then subjected to ultracentrifugation at 100,000 $\times$ g for 90 min at 4 °C. The resulting

exosome pellet was resuspended in PBS and stored at –80 °C for subsequent use.

## 2.6. Preparation of f-exo

The BCA Protein Quantification Kit is used to determine the protein concentration in exosomes. M2-exo was mixed with USC-exo and subjected to ultrasonic membrane fusion using a SCIENTZ-IID Ultrasonic Homogenizer (Ningbo Scientz Biotechnology Co., Ltd, China.) for 3 min. This was followed by repeated co-extrusion with the polycarbonate membrane of the liposome extruder (100 nm, 50 nm), forming the f-exo.

## 2.7. Transmission electron microscopy (TEM)

f-exo morphology was analyzed by TEM. 10  $\mu$ L f-exo was placed onto a carbon-coated copper grid and allowed to adsorb for 15 min. The grid was then stained with 2 % phosphotungstic acid for 5 min to enhance contrast. After drying, the grid was examined under a TEM at 80 kV. Images were captured to observe the typical cup-shaped morphology of exosomes.

## 2.8. Nanoparticle tracking analysis (NTA)

The size distribution and concentration of exosomes were determined by NTA. A diluted f-exo sample was introduced into the NTA system, and video recordings were taken to track the Brownian motion of individual particles. The data were analyzed using NTA software to determine the mean particle size and concentration of f-exo.

## 2.9. Nano flow cytometry

Flow cytometry (VSSC mode) was used to analyze the efficiency of fusion preparation of f-exo by fusion of M2-exo and USC-exo with different protein ratios. Cell membrane fluorescent dyes DiI and DiO working solutions were prepared to label M2-exo and USC-exo, respectively, and 100 kDa ultrafiltration tubes were used to remove excess fluorescent dyes. A liposome extruder was used to prepare f-exo with different protein ratios (M2-exo: USC-exo = 3:1, 2:1, 1:1, 1:2, 1:3), and the acquisition parameters PE-DiI and FITC-DiO were set to calculate the ratio of PE and FITC double positivity (f-exo ratio).

## 2.10. FRET

The fusion of M2-exo with USC-exo was verified by FRET assay. Briefly, M2-exo was labeled with DiO (FRET donor) and DiI (FRET acceptor), and then M2-exo was simply mixed with USC-exo or f-exo was prepared, and the fluorescence spectra of mixed exosome versus f-exo were analyzed by multifunctional zymography. The fluorescence recovery at 534 nm was observed with the FRET signal attenuation at 583 nm to indicate the intercalation of the two exosomes, and the average decrease in FRET efficiency of mixed exo was compared with that of f-exo.

## 2.11. Western blotting analysis

Exosomes or cell samples were lysed by RIPA, and the concentration of each sample was calculated according to the BCA protein quantification results. The volume of the sample in each well was calculated according to the amount of 20  $\mu$ g of protein per well. Electrophoresis was accomplished by using a 10 % sodium dodecyl sulfate polyacrylamide gel electrophoresis preparation kit (Shandong Sparkjade Biotechnology Co., Ltd.) and Tris-Gly running buffer. The PVDF membrane was wetted and activated in methanol and then equilibrated in the transfer solution for at least 5 min. The transfer current was set to a constant current, 400 mA, for 20 min. The membrane was blocked by Western Quick Block Kit (GenScript) on a room temperature shaker for

10–20 min, washed with TBST, and then incubated with diluted primary antibody overnight at 4 °C. The membrane was then washed with TBST, then incubated with diluted corresponding secondary antibody for 1 h at room temperature. After washing with TBST, the expression of the target proteins was detected using the ECL Prime Western Blotting System (Absin). The quantification of the proteins was performed using Image Lab software.

## 2.12. Colocalization analysis

The RAW264.7 cells were cultured until they reached 70 % density, and  $2 \times 10^4$  RAW264.7 cells were seeded into confocal dishes and placed in the incubator overnight. The working solution of lipophilic dye DiO and DiI was prepared according to the instructions. The lipophilic dye DiI was used to label the M2-exo, and the lipophilic dye DiO was used to label the USC-exo. The incubation was performed at room temperature and protected from light for 30 min. Then the exosomes were transferred to 0.5 mL ultrafiltration tubes (100 kDa), subjected to centrifugation at 4 °C and 10,000 rpm for 10 min, and the ultrafiltrate was washed with PBS and then subjected to another round of centrifugation. M2-exo was briefly mixed with USC-exo, or f-exo was prepared. 100 µg of the mixed exo or f-exo was introduced to RAW264.7 cells respectively, and incubated for 4 h in a cell culture incubator, protected from light. The medium was then discarded, the cells were washed with PBS, and they were fixed with 4 % PFA for 10 min. The cells were subsequently washed with PBS and incubated with DAPI solution for 10 min. Subsequently, the cells were washed with PBS, and the antifading mounting medium was added. The localization between the green DiO signals (USC-exo) the red DiI signals (M2-exo) and the blue DAPI signals (cell nucleus) was observed under a laser scanning confocal microscope. The localization between the signal (nucleus)

## 2.13. Osteoblast differentiation

The P1 BMSCs were inoculated into the corresponding well plates and cultured overnight. The cells were then induced to differentiate into osteoblasts using the osteogenic differentiation medium. The experimental group was treated with M2-exo, USC-exo (100 µg/mL), or a combination of both. Furthermore, f-exo interventions were conducted on the original basis. ALP staining, ARS staining, and Sirius red staining were employed to analyze the osteogenic differentiation of the BMSCs. Additionally, immunofluorescence and Western blotting were utilized to analyze the expression levels of proteins related to osteoblast differentiation. The osteogenic differentiation of BMSCs was analyzed through ALP staining, ARS staining, and Sirius red staining. Moreover, the expression level of osteoblast differentiation-related proteins was analyzed through immunofluorescence and Western blotting.

## 2.14. Osteoclast differentiation

BMDM were inoculated into the corresponding well plates and cultured overnight. Osteoclasts were induced to differentiate with the complete medium containing 100 ng/mL RANKL (CatC28A; Novoprotein, Shanghai, China). The experimental group was treated with M2-exo, USC-exo (100 µg/mL), mixed exo, and f-exo. To gain further insight, TRAP staining was employed to assess the number and area of osteoclasts, while f-exo staining was utilized to evaluate the arrangement of the podosome in these cells. Additionally, qPCR and Western blotting were conducted to analyze the expression levels of genes and proteins associated with osteoclast differentiation. The number and area of osteoclasts were analyzed through TRAP staining, while f-actin staining was employed to assess the arrangement of the podosome of osteoclasts. Additionally, qPCR and Western blotting were utilized to analyze the expression levels of genes and proteins related to osteoclast differentiation.

## 2.15. Real-time qPCR

Total RNA was extracted from treated samples using the Total RNA Extraction Kit, and cDNA was synthesized using the Reverse Transcriptase Kit (GeneCopoeia). Real-time qPCR was conducted on a CFX Connect Real-Time System with HotStart 2X SYBR Green qPCR Master Mix, by the manufacturer's instructions. Primers were designed to target specific genes, and glyceraldehyde-3-phosphate dehydrogenase (Actin) was employed as an internal reference gene for data normalization. The  $2^{-\Delta\Delta Ct}$  method was employed to calculate the relative expression levels of the target genes, thereby assessing the impact of fused exosomes (f-exo) on the expression of the pertinent genes.

## 2.16. Wound healing assay

HUEVCs in the logarithmic growth phase were taken and inoculated in 6-well plates at a density of  $1 \times 10^6$  cells/well, and three biological replicates were set up for each group. The cells were incubated at 37 °C under 5 % CO<sub>2</sub> until the cell fusion reached about 90 %. Subsequently, a sterile 10 µL pipette tip was employed to create a "cross-shaped" scratch in the center of each well along a pre-marked straight line. The wells were then washed with PBS to remove any cellular debris that may have accumulated around the edges of the scratches. The cells were subsequently treated with the culture medium containing 1 % fetal bovine serum (Inner Mongolia Wanrui Biotechnology Co., Ltd.) and varying types of exosomes. Images of the scratches were captured using an inverted microscope, with 0 h marking the commencement of the experiment. The cells were returned to the incubator to resume incubation, with subsequent scratch images obtained after 12 and 24 h, respectively. The impact of exosomes on the migratory capacity of the cells was evaluated by quantifying the change in the scratch area of each group of cells using ImageJ software.

## 2.17. Transwell assay

The HUEVCs were subjected to a 12-h starvation period. The cells were then resuspended using serum-free DMEM medium, and the cell density was adjusted to  $6 \times 10^5$  cells/mL. A total of 200 µL of cell suspension, containing approximately  $1.2 \times 10^5$  cells, was added to the Transwell insert. The lower chamber was supplemented with 600 µL of complete medium containing the corresponding treatments, which were allocated to the following groupings: control group, M2-exo group, USC-exo group, mixed exo group, and f-exo group. The samples were incubated for 24 h at 37 °C with 5 % CO<sub>2</sub>. Following the incubation period, the Transwell was washed twice with PBS. Subsequently, 4 % PFA was added to the device for 15–20 min to facilitate cell fixation. The cells were then washed a second time with PBS to remove any residual PFA. Subsequently, 400 µL of 1 % crystal violet solution was added to stain the migrating cells for 30 min. Once the staining process was complete, the Transwell chambers were washed three times with water to remove any residual dye. The upper surface of the chambers was then gently wiped with a moistened cotton swab to remove any non-migrated cells. The chambers were subsequently transferred to an area with adequate ventilation to facilitate the natural drying process. Subsequently, the number of migrated cells was quantified through microscopic observation, with five randomly selected fields of view counted and subjected to statistical analysis.

## 2.18. Tube formation assay

Before the commencement of the experiment, all the requisite items were pre-cooled in a refrigerator set at –20 °C, and the entire experiment was conducted on ice. The Matrigel should be thawed on ice overnight. Thereafter, 100 µL of Matrigel gel should be added to the wells of a 48-well plate, ensuring that it is evenly distributed at the bottom of the wells to prevent the formation of air bubbles. The plate



was stored in a refrigerator set at 4 °C for 2 h, to achieve the flattest possible surface for the gel. Subsequently, the plates were transferred to an incubator maintained at 37 °C to facilitate the solidification of the gel. Following digestion, centrifugation, and resuspension, HUEVCs were inoculated into the wells lined with Matrigel glue at a density of  $4 \times 10^4$  cells per well. The complete medium containing each group of exosomes was then added for intervention. The wells were incubated in an incubator at 37 °C, and the aggregation of HUEVCs on Matrigel glue was observed at 4 h, 6 h, and 8 h after cell inoculation. Images were collected at the appropriate time points using a light microscope. A Calcein-AM fluorescent staining solution was prepared for the staining of live cells, and images were acquired. The images were then analyzed using ImageJ software, with the lumen formation parameters quantified in three randomly selected regions.

### 2.19. Calvarial osteolysis models

8–10 week-old male C57BL/6J mice were selected as experimental subjects and were rendered unconscious through the administration of sodium pentobarbital (50 mg/kg) via intraperitoneal injection. During the surgical procedure, the mice were maintained at a constant body temperature and an appropriate depth of anesthesia. The scalp was incised along the midline to expose the skull bilaterally. The periosteum on the surface of the skull was meticulously removed to prevent injury to the subcutaneous tissue. Thirty milligrams of titanium abrasion particles (Thermo Fisher Scientific Inc., USA) were strategically positioned on the cranial surface, ensuring uniform distribution to simulate the process of osteolysis. Subsequently, the wound was meticulously closed using 4-0 Prolene sutures to guarantee optimal wound closure. Appropriate antibiotics were administered postoperatively to prevent infection, and the mice were closely monitored to ensure successful recovery.

### 2.20. In vivo imaging system

C57BL/6J male mice of 8–10 weeks of age were selected as experimental subjects, and a titanium-induced mouse cranial osteolysis model was established. Following the establishment of the model, a single dose of DiR-labeled USC-exo, mixed exo, M2-exo, and f-exo (200 µg) was administered via the tail vein. Subsequently, fluorescence images were acquired using IVIS at 12 h, 24 h, 36 h, 48 h, and 60 h, and the fluorescence intensity in the cranial region was analyzed. Subsequently, the mice were euthanized at the 60-h mark, and the cranium and major organs were excised. The distribution of f-exo in the cranium and other major organs was then subjected to further analysis to assess its targeting and distribution properties in vivo.

### 2.21. Micro-CT analysis

The mouse skulls were removed and fixed, and the processed skulls were scanned in three dimensions using micro-CT with the scanning parameters set at 50 kV, 500 µA, and a resolution of 6.5 µm. The microstructure of the skulls was discernible upon reconstruction of three-dimensional images derived from the acquired data. Subsequently, the reconstructed images were subjected to quantitative analysis using specialized software, including the measurement of the ratio of bone surface (BS) to bone volume (BV), the ratio of BV to total volume (TV), and the total porosity.

### 2.22. H&E staining and histomorphometric analysis

The cranial samples of the mice were fixed in 4 % paraformaldehyde for 24 h, after which decalcification was initiated by immersing the samples in 0.5 M EDTA (pH 7.2) for one week. Following the completion of decalcification, the samples were subjected to a series of concentration gradients of ethanol for dehydration. They were then immersed in xylene for clearing and finally embedded in paraffin, resulting in the

production of 5 µm thick sections. The sections were then subjected to a staining procedure involving the use of hematoxylin, followed by a differentiation step utilizing hydrochloric alcohol to enhance the contrast of the nuclei. This was subsequently followed by a counterstaining process with ammonia, which served to restore the natural tone of the cytoplasm. Finally, the sections were restained with eosin, which served to emphasize the cytoplasmic structures. The sections were then blocked using neutral gum. The morphological alterations in the tissues were evaluated through digital scanning of the sections.

### 2.23. Immunofluorescent staining

Paraffin-embedded sections were first deparaffinized with xylene and rehydrated by gradient alcohol solution. The appropriate antigen repair solution was selected according to the instructions of the primary antibody and heat-induced antigen repair was performed using an autoclave. The nonspecific binding sites were closed with 5 % bovine serum albumin for 1 h at room temperature. Sections were subsequently co-incubated with primary antibodies overnight at 4 °C. After returning to room temperature the following day, the sections were incubated with the corresponding fluorescently labeled secondary antibodies for 1 h at room temperature, and finally, the nuclei were restained with DAPI. After sealing the sections, they were observed using a fluorescence microscope and recorded images were taken. Positive signal area and intensity analysis was then done by ImageJ software.

### 2.24. Exosome proteomic analysis instrument and conditions

Each component underwent separation using the nanoElute liquid chromatography system by Bruker. Mobile phase A consisted of a 0.1 % formic acid solution in water, while mobile phase B contained 0.1 % formic acid in acetonitrile. The gradient elution conditions were as follows: 0–45 min, 2–22 % B; 45–50 min, 22–37 % B; 50–55 min, 37–80 % B; 55–60 min, 80 %. Subsequent to chromatographic separation by the ultra-high-performance liquid chromatography system, the peptides were injected into the timsTOF Pro mass spectrometer manufactured by Bruker for analysis. The mass spectrometry parameters were set as follows: the capillary voltage was maintained at 1500V, with primary and secondary scan ranges spanning from 100 to 1700 *m/z*, and ion mobility windows (1/K0) ranging from 0.7 to 1.3 Vs/cm<sup>2</sup>. For processing the original DIA data, the Spectronaut Pulsar software was employed with fixed Carbamidomethyl © modification, variable Oxidation (M), and Acetyl (N-term) modifications, allowing for a maximum of 2 missed cleavage sites. Differential protein analysis entailed the assessment of Biological Processes (BP), Cellular Components (CC), and Molecular Functions (MF) utilizing the Gene Ontology (GO) database. The Kyoto Encyclopedia of Genes and Genomes (KEGG) database was employed to investigate the primary pathways related to differentially expressed proteins. Furthermore, the protein-protein interaction (PPI) analysis was based on the STRING database, leading to the development of a differential protein interaction network.

### 2.25. Statistical analysis

To ensure the reliability of the results, all in vitro experimental data in this study were independently repeated three times, and in vivo experimental data were independently repeated five times. The experimental data were presented as mean ± standard deviation and subjected to statistical analysis using GraphPad Prism 9, ImageJ, and Image Lab software. A one-way analysis of variance (ANOVA) was employed to make multiple group comparisons. A statistical significance level of  $P < 0.05$  was employed, with the symbols "ns" (non-significant) and " $*P < 0.05$ " ( $P < 0.05$ ) and " $***P < 0.01$ " ( $P < 0.01$ ) used to denote the degree of significance. The symbols " $****P < 0.001$ " were employed to distinguish between the various levels of statistical significance.

### 3. Result

#### 3.1. Preparation and characterization of f-exo

Exosomes are a highly promising class of drug delivery vehicles and therapeutic tools, exhibiting unique biological properties that make them well-suited for a range of applications. In this study, we developed an innovative exosome-targeted delivery method, namely the construction of M2-exo and USC-exo fused exosomes (f-exo), for targeted delivery of therapeutic exosomes to the periprosthetic osteolysis region. To prepare f-exo, we cultured and identified M2 macrophages and USC (Figs. S1A and B) to collect culture supernatants of M2 macrophages and USC, then isolated exosomes using ultracentrifugation. The fusion efficiency of f-exo prepared with different initial ratios of M2-exo/USC-exo was first explored. By labeling M2-exo with DiI and USC-exo with DiO, it was determined that the percentage of double-positive particles was significantly higher in the fusion sample f-exo than in the mixed sample mixed exo, as evidenced by nano flow cytometry (Fig. 1A). It is noteworthy that the highest percentage of double positives was observed at an initial ratio of 1:1 M2-exo/USC-exo (Fig. 1B). Furthermore, the fusion of M2-exo/USC-exo was verified by FRET assay (Fig. 1C). Transmission electron microscopy (TEM) observations revealed that the exosomes

exhibited a typical tea-saucer-like vesicle morphology, whereas the f-exo displayed a well-structured and intact disk-like vesicle (Fig. 1D). Western blotting analysis demonstrated the presence of the exosome signature proteins CD63 and TSG101 in M2-exo, USC-exo, and f-exo, while the endoplasmic reticulum protein Calnexin was not expressed (Fig. 1E). The Coomassie Brilliant Blue staining demonstrated that f-exo exhibited protein expression profiles analogous to those of both M2-exo and USC-exo (Fig. S1). This finding suggests that the protein composition of the two exosomes was preserved during the preparation of f-exo. Meanwhile, protein extracted from M2-exo, USC-exo, and f-exo to map the proteomic landscape. Gene Ontology (GO) classifications of three groups associated with cellular components were characterized to clarify these sources of protein, which indicated all three groups of proteins were derived from exosomes (Fig. 1F–S5B). At the same time, all the detected proteins were analyzed using a venn diagram, and it was found that almost all the proteins in the f-exo group were derived from both M2-exo, and USC-exo, which demonstrated that f-exo was able to retain proteins from both M2-exo and USC-exo sources (Fig. 1G). To test the physiological stability of f-exo, we examined the zeta potential of f-exo stored at  $-80^{\circ}\text{C}$  for different times, and the results showed that f-exo was still able to maintain stability after 90 days of storage (Fig. 1H). The average particle size of M2-exo and USC-exo was found to be within the

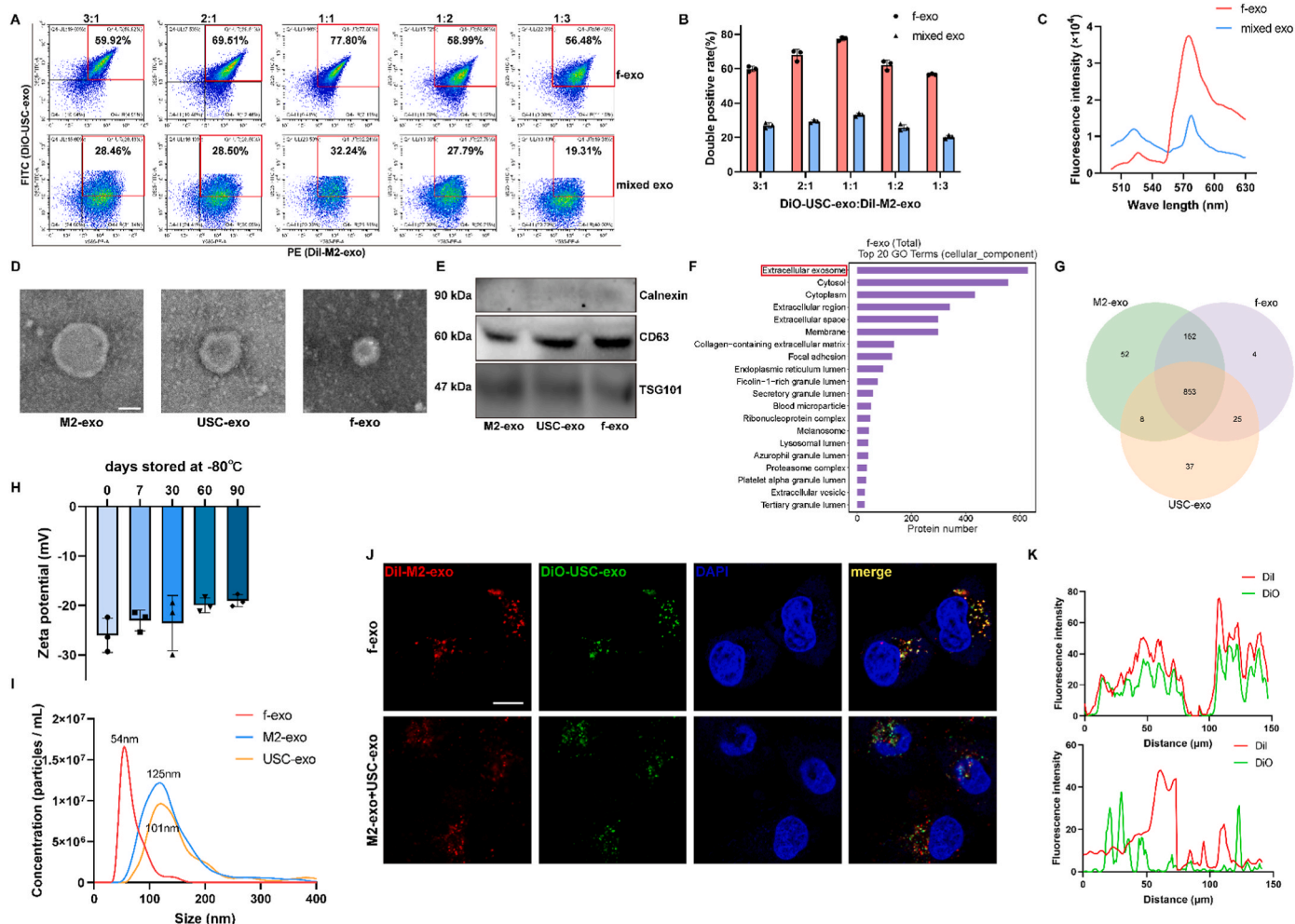


**Fig. 1. Preparation and characterization of f-exo** (A, B) Double labeled ratio of f-exo and mixed exo analyzed by Flow cytometry (VSSC mode). (C) Fluorescence intensity of DiO and DiI double labeled exo in FRET assay. (D) TEM images of M2-exo, USC-exo and f-exo. Scale bar, 50 nm. (E) Western blotting assay of CD63, TSG101 and Calnexin expression in M2-exo, USC-exo and f-exo. (F) GO Enrichment analysis of f-exo in cellular component category (G) Venn diagram of M2-exo, USC-exo and f-exo. (H) Zeta potential of f-exo stored at  $-80^{\circ}\text{C}$  in 0, 7, 30, 60, 90 days. (I) Size distribution of M2-exo, USC-exo and f-exo analyzed by NTA. (J) Characterization of M2-exo, USC-exo and f-exo under CLSM. Scale bar, 10  $\mu\text{m}$ . (K) Co-localization analysis of CLSM image. DiI (red) labeled M2-exo, DiO (green) labeled USC-exo before fusing or mixing.

range of 100–130 nm, as determined by nanoparticle tracking analysis. In contrast, f-exo prepared by liposome extrusion exhibited a more homogeneous particle size of approximately 54 nm (Fig. 1I). This finding suggests that the fusion-prepared f-exo retained the typical exosome properties (Fig. 1I). The cellular localization of f-exo was observed using laser scanning confocal microscopy. f-exo was prepared by fusion of DiI-M2-exo and DiO-USC-exo or simply mixed and then co-incubated with RAW264.7 cells. The confocal images demonstrated that the green and red signals were separated in the mixed exo group, whereas the fluorescent signals exhibited co-localization in the f-exo group (Fig. 1J and K).

This finding suggests that the f-exo was capable of entering the cells with high efficiency and exhibited good co-localization within the cells. In conclusion, the fused exosome f-exo of M2-exo and USC-exo was successfully prepared by ultrasound in conjunction with a liposome extruder, and the protein composition of both exosomes was preserved.

### 3.2. Regulation of bone metabolic homeostasis by f-exo in vitro

To investigate the effect of f-exo on osteogenic differentiation of BMSCs, this study assessed ALP expression, calcium nodule formation, and collagen production during osteogenic differentiation using alkaline phosphatase (ALP) staining, alizarin red S (ARS) staining, and Sirius red staining (Fig. 2A). The results showed that both M2-exo and USC-exo enhanced ALP expression, calcium nodule formation, and collagen production during osteogenic induction. The mixed exo and f-exo treatment groups exhibited a more pronounced promotion. A quantitative analysis corroborated the intergroup differences in the absorbance of the eluate after ARS staining and Sirius red staining, which were consistent with the aforementioned staining results (Fig. 2E and F). Furthermore, the intracellular collagen production following exosome treatment was corroborated by immunofluorescence staining of collagen 1 $\alpha$  (Col1a) and quantitative analysis of fluorescence intensity (Fig. 2B–D). Both M2-exo and USC-exo facilitated the production of type I collagen to a certain extent during osteogenic induction of BMSCs, whereas mixed exo and f-exo promoted more significant collagen production. Western blotting was employed to ascertain the expression levels of the pivotal transcription factors RUNX2 and sp7 proteins throughout the osteogenic differentiation process. The quantitative analysis revealed that the mixed exo and f-exo groups exhibited elevated expression levels of RUNX2 and sp7 in comparison to the M2-exo or USC-exo groups (Fig. 2C–G, H). In conclusion, f-exo markedly enhanced the differentiation of BMSCs into osteoblasts.

To further evaluate the effect of f-exo on exogenous RANKL-induced osteoclastic differentiation of macrophages, a series of assays were conducted, including tartrate-resistant acid phosphatase (TRAP) staining and activity assay, fluorescent staining, and flow cytometry for reactive oxygen species (ROS), and f-actin/DAPI staining. These assays were employed to assess the formation of osteoclasts, the generation of ROS, and the arrangement of the osteoclast podosome. The TRAP staining and activity assay with subsequent quantitative analysis demonstrated that the combination of exo and f-exo markedly diminished the number of TRAP-positive osteoclasts (Fig. 3A–C). Osteoclasts induced by RANKL exhibited F-actin arranged in dense podosome belts, whereas mixed exo and f-exo-treated osteoclasts displayed a more dispersed podosome structure (Fig. 3D). The ROS fluorescence intensity detected by fluorescent microscopy and flow cytometry was markedly diminished in the mixed exo and f-exo groups relative to the M2-exo or USC-exo groups, indicating that mixed exo and f-exo were capable of substantially impeding the signaling processes associated with osteoclast differentiation. (Fig. 3E–G). The expression levels of key genes and proteins during osteoclast differentiation were further analyzed. The Western blotting results indicated that mixed exo and f-exo significantly inhibited the expression levels of NFATC-1, TRAP, and CTSK protein (Fig. 3H–I). Additionally, the qPCR assay demonstrated that mixed exo and f-exo significantly down-regulated the expression levels of *MMP9*,

*OSCAR*, and *NFATC-1* mRNA (Fig. 3J). Notably, the effects were more pronounced than those observed in the exosome alone group. The aforementioned results demonstrated that f-exo exerted an inhibitory effect on osteoclast differentiation, maturation, and function of both M2-exo and USC-exo. Further investigation is required to elucidate the impact of f-exo on angiogenesis. To initially assess the impact of f-exo on the migratory capacity of HUEVCs, we employed a cell scratch assay and Transwell migration assay. As illustrated in Fig. 4A, following 12 h of scratching, the scratch healing was more pronounced in the M2-exo and USC-exo groups relative to the control group. Conversely, the scratch healing was more substantial in the mixed exo and f-exo groups. At 24 h, the scratches in the mixed exo and f-exo groups exhibited complete healing, whereas the scratches in the M2-exo and USC-exo groups demonstrated partial healing, with the wounds narrowing but not fully closing (Fig. 4B and C). The results of the Transwell migration assay and quantitative analysis (Fig. 4D and E) demonstrated that mixed exo and f-exo were capable of significantly enhancing the migration ability of HUEVCs, with a more pronounced effect than that observed in the M2-exo and USC-exo groups. In light of the aforementioned results, we sought to further investigate the impact of f-exo on the tubule formation capacity of HUEVCs. Following an 8-h incubation period, the mixed exo and f-exo groups exhibited enhanced tubule formation, while the M2-exo and USC-exo groups demonstrated cell aggregation and protruding pseudopods, albeit with less pronounced tube formation (Fig. 4F). The quantitative analysis of the number of branches (Fig. 4G) and loops (Fig. 4H) formed by the tubules of HUEVCs using Image J software provided further confirmation of the trend observed under the microscope ( $P < 0.05$ ). The results of the Western blotting experiments and quantitative analysis (Fig. 4I and J) demonstrated that the mixed exo and f-exo groups significantly enhanced the expression of angiogenesis-related proteins CD31, EMCN, VEGF, and HIF1 $\alpha$ . Therefore, it can be concluded that f-exo demonstrated a greater capacity to stimulate angiogenesis in HUEVCs.

### 3.3. Targeting of f-exo to areas of periprosthetic osteolysis

To evaluate the capacity of f-exo to target the periprosthetic osteolytic region in vivo, a Ti particle-induced cranial osteolysis model in mice was employed in this study. The distribution of exosomes in vivo was monitored by labeling f-exo with DiR, a cell membrane fluorescent dye, and by conducting in vivo fluorescence imaging with the aid of IVIS. As illustrated in Fig. 5A and E, fluorescence images were obtained at various time points (12 h, 24 h, 36 h, 48 h, and 60 h) following the tail vein injection, and the fluorescence intensity of the cranial region was quantified. The DiR group was employed as a negative control to exclude the fluorescence effect of the dye itself. The USC-exo group exhibited a diminished fluorescence signal in the osteolysis region. At 36 h, the fluorescence intensity of the f-exo and M2-exo groups exhibited a marked increase, reaching threefold ( $P < 0.05$ ) that of the USC-exo group and 2.5 times ( $P < 0.05$ ) that of the mixed exo group, respectively. This suggests that f-exo significantly enhanced the aggregation of USC-exo in the region of osteolysis, compared with simple mixing. Following a 60-h observation period, the mice were euthanized, and the skull slices were removed for direct observation of the fluorescence intensity in the osteolysis region and quantitative analysis (Fig. 5B–F). The results of the in vivo fluorescence imaging was consistent with those of the exosome analysis, indicating that the fluorescence intensity of the f-exo and M2-exo groups in the region of osteolysis was approximately five times higher than that of the USC-exo group and 2.5 times higher than that of the mixed exo group, respectively ( $P < 0.05$ ). Further analysis of the distribution of f-exo in major organs revealed the presence of higher f-exo and M2-exo fluorescence signals in the liver and spleen, indicating that f-exo and M2-exo decreased the clearance rate of exosomes alone and prolonged their circulation time in vivo (Fig. 5C–G). These findings demonstrate that f-exo exhibits the same regional targeting and prolonged circulation as M2-exo, effectively prolonging the



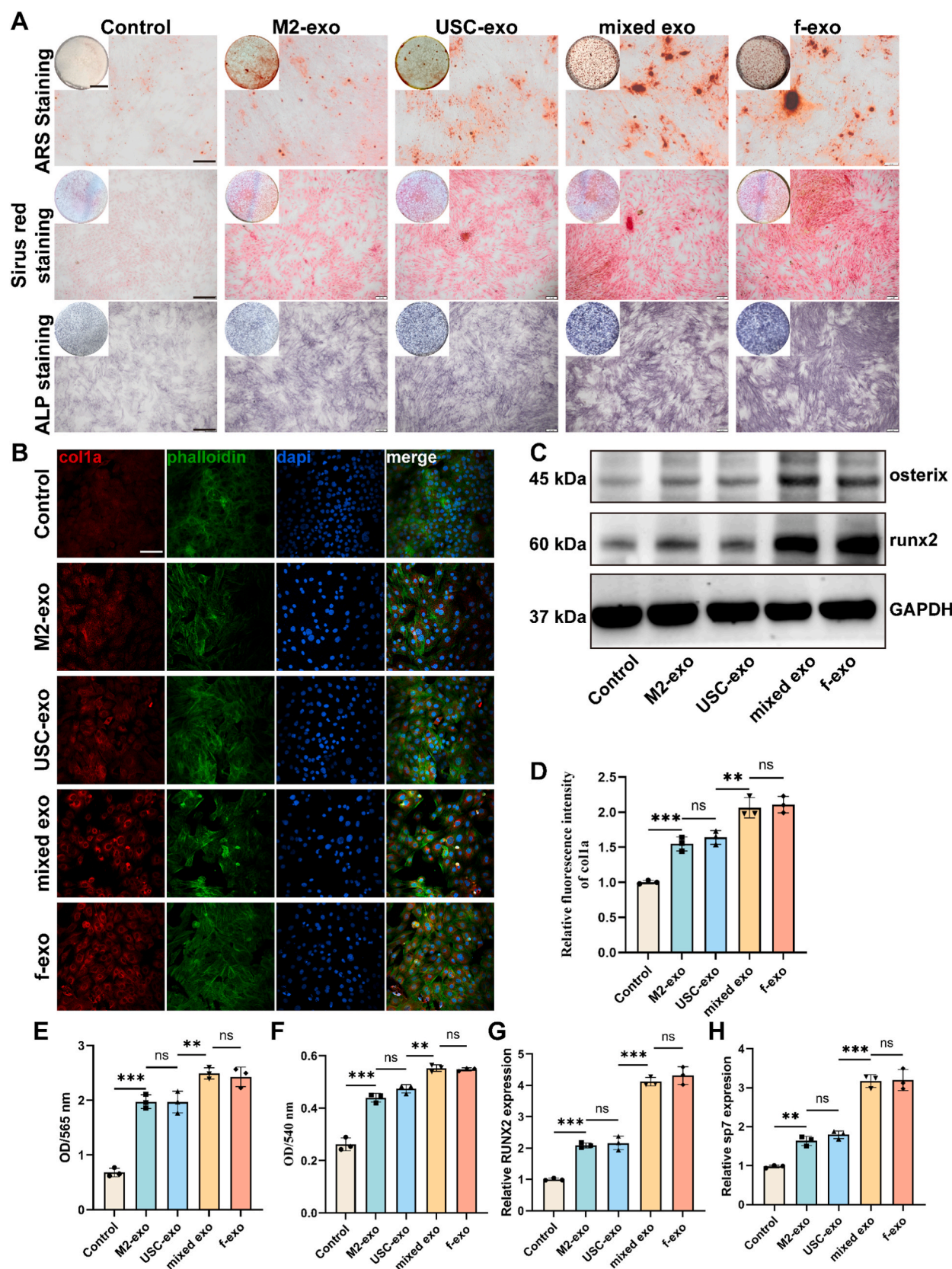


**Fig. 2.** Regulation of osteoblast differentiation by f-exo in vitro (A, E-F) Osteogenesis of BMSC induced by f-exo in vitro assessed by ARS, sirius red staining, ALP staining, and their quantifications. Scale bar 3 mm, 400  $\mu$ m (enlarged) (B, D) the intracellular collagen production assessed by immunofluorescence staining of collagen 1 $\alpha$  (Col1a) and quantitative analysis of fluorescence intensity. Scale bar, 200  $\mu$ m (C, G-H) Osteogenic-related protein analyzed by western blotting, and its relative quantifications (The data in the figures represent the averages  $\pm$  SD,  $n = 3$  samples per group,  $^*P < 0.05$ ,  $^{**}P < 0.01$ ,  $^{***}P < 0.001$ ).

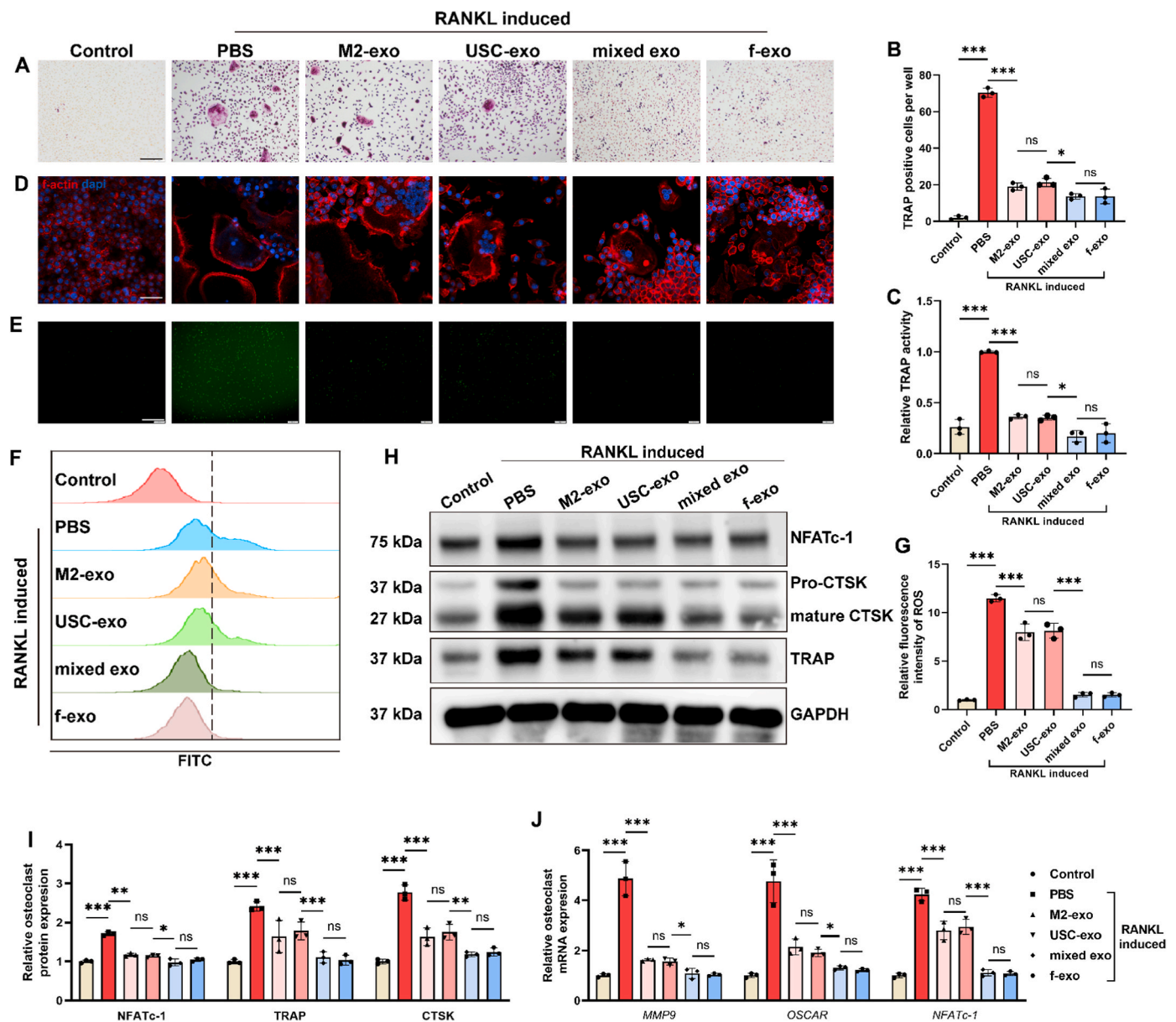


**Fig. 3. Regulation of osteoclast by f-exo in vitro** (A, B) The TRAP staining and its quantification. (C) Relative TRAP activity, (D) f-actin staining, (E) fluorescent staining and (F, G) flow cytometric for ROS detection of BMDM induced by RANKL with or without exosomes. (H, I) Osteoclast related protein expression demonstrated by western blotting. (J) Osteoclast related mRNA expression demonstrated by qRT-PCR. (Scale bar, 100  $\mu$ m). The data in the figures represent the averages  $\pm$  SD, n = 3 samples per group, \* $P$  < 0.05, \*\* $P$  < 0.01, \*\*\* $P$  < 0.001).

exogenously applied exosomes' circulation time in vivo. Meanwhile, we investigated the in vivo distribution of f-exo in calvarial osteolysis model mice by intravenous injection of DiI-labeled f-exo, and performed ivis organ and calvaria imaging at 5, 12, 24, 36, 48, 60, 120, and 168 h, respectively. As illustrated in Figure D, H, and I, the results demonstrated that the fluorescence signal of f-exo in the skull attained its maximum level at the 36th hour and subsequently decreased over time, reaching a nadir of 1/4 of the initial value after 168 h. In contrast, the fluorescence signals in the blood sinusoid-rich organs, such as the liver and the spleen, remained at a higher level throughout the 168-h period. This provides a foundation for the treatment of periprosthetic osteolytic diseases.

### 3.4. Effect of f-exo against periprosthetic osteolysis in vivo

Finally, we investigated the impact of f-exo on periprosthetic osteolysis in vivo. Histological examination of major organs using the

H&E staining method and mouse blood biochemical assay confirmed the safety of f-exo in vivo (Figs. S2A and B). Micro-CT results (Fig. 6A) revealed a significant effect of f-exo in the treatment of osteolysis. In comparison to the sham group, the Ti particles group exhibited notable osteolysis alterations in Micro-CT 3D reconstruction images, as indicated by a considerable reduction in BV/TV and a notable increase in BS/BV and total porosity. Despite the USC-exo group demonstrating superior bone metabolism modulation effects in vitro, it was unable to impede the osteolysis process in vivo due to the absence of specific targeting effects. In contrast, the M2-exo group demonstrated a certain degree of alleviation of the osteolysis phenomenon. This outcome may be attributed to the effective targeting of the osteolysis region by M2-exo. It is noteworthy that the simple mixing of M2-exo and USC-exo did not yield comparable results. In contrast, the f-exo group demonstrated precise targeting and a significant inhibitory effect on osteolysis, exhibiting a significantly higher BV/TV than the M2-exo and USC-exo groups. Conversely, the BS/BV and total porosity were significantly



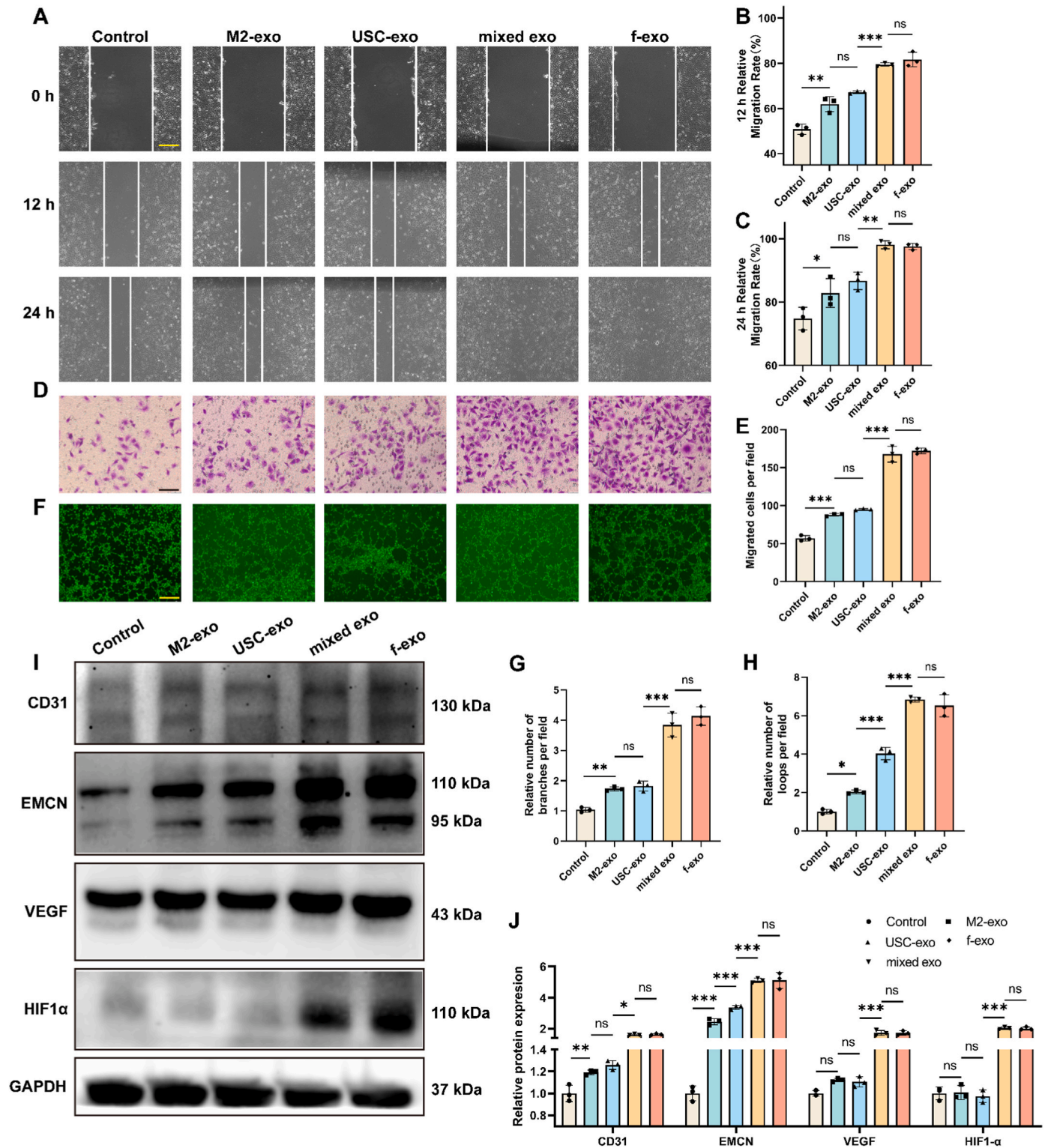


**Fig. 4.** Regulation of bone metabolic homeostasis by f-exo in vitro. Angiogenesis of HUVEC treated with exosomes assessed by (A–C) wound healing assay (Scale bar, 200  $\mu$ m) (D–E) transwell migration assay (Scale bar, 100  $\mu$ m), and (F–H) tube formation assay. (Scale bar, 400  $\mu$ m). (I–J) Angiogenesis related protein expression demonstrated by western blotting, and its relative quantifications. (The data in the figures represent the averages  $\pm$  SD,  $n = 3$  samples per group, \* $P < 0.05$ , \*\* $P < 0.01$ , \*\*\* $P < 0.001$ ).

lower than those of the M2-exo and USC-exo groups (Fig. 6B, C, D).

As illustrated in Fig. 7A, the H&E staining revealed a notable infiltration of inflammatory cells in the cranial region where Ti particles had induced an inflammatory response. This infiltration resulted in structural alterations to the normal bone tissue, accompanied by an increase

in the thickness of the inflammatory periosteum. However, following the f-exo intervention, there was a restoration of bone tissue morphology and a significant reduction in the level of inflammation. Fig. 7F illustrates the quantitative analysis of periosteal thickness, which corroborates the observations made through H&E staining. The role of f-exo in

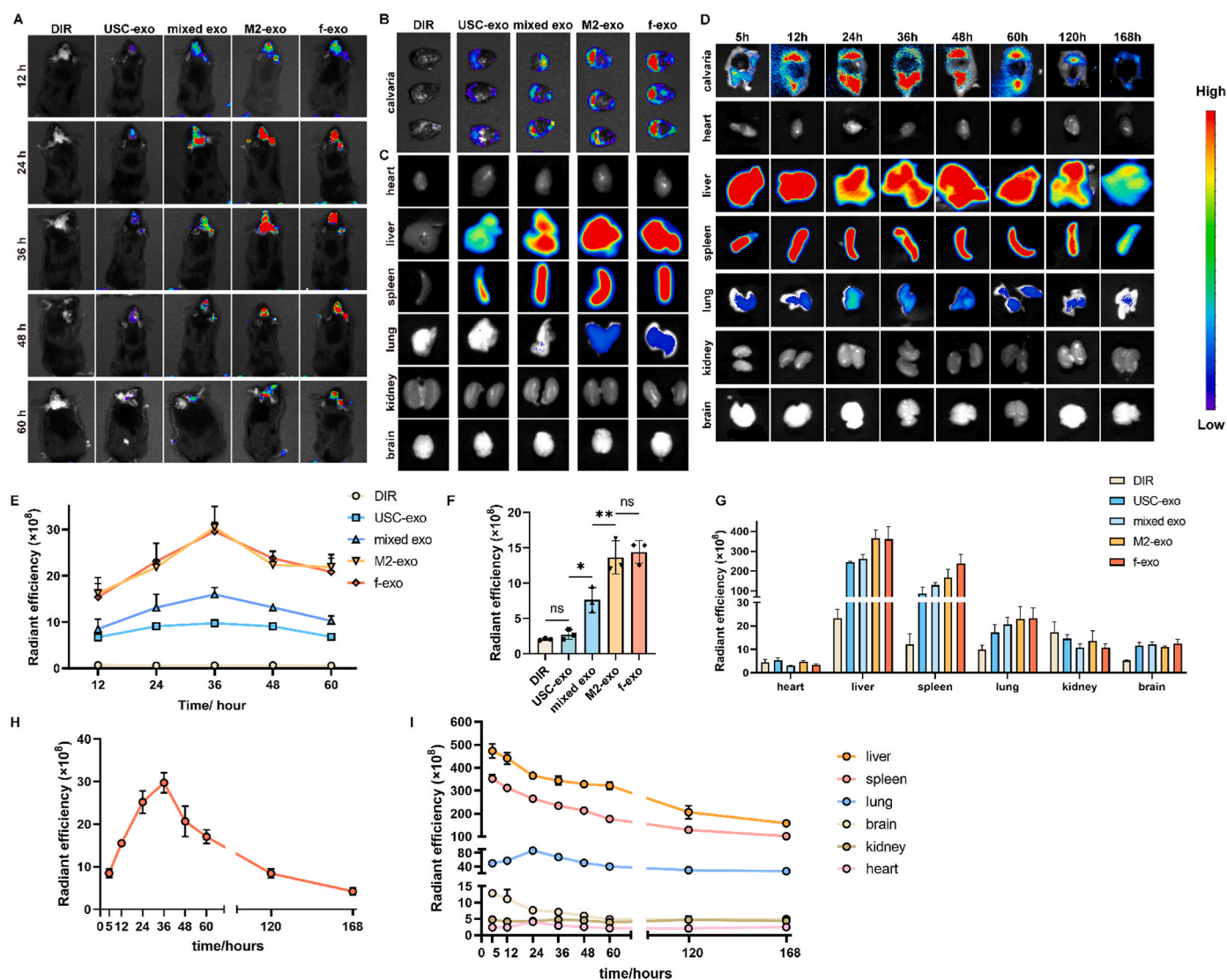


**Fig. 5.** Targeting of f-exo to areas of periprosthetic osteolysis (A, E) The IVIS images and quantification of fluorescent intensity of the DiR labeled exo in 12h, 24h, 36h, 48h, and 60h. (B) The exosome distribution of the calvaria region and (C) major organ of the mouse, and (F, G) their quantification of fluorescent intensity. (D) The f-exo distribution of the calvaria region and major organ of the mouse in 5h 12h, 24h, 36h, 48h, 60h, 120h, and 168h (H, I) their quantification of fluorescent intensity. (The data in the figures represent the averages  $\pm$  SD,  $n = 3$  samples per group,  $P < 0.05$ ,  $**P < 0.01$ ,  $***P < 0.001$ ).

inhibiting osteoclast formation in the region of Ti particle-induced osteolysis, thereby reducing bone resorption activity, was further confirmed by TRAP staining (Fig. 7B). Fig. 7E illustrates the quantitative analysis results of the TRAP-positive regions, thereby corroborating the pronounced ameliorative impact of the f-exo group, particularly in the context of osteoclast activity inhibition. To evaluate the impact of f-exo on the osteogenic and angiogenic potential of the osteolysis region, we conducted an immunofluorescence analysis. The findings revealed that f-exo markedly enhanced the expression of CD31 and EMCN, H-vessel-related proteins (Fig. 7C). H-vessels are specialized vascular structures that play a pivotal role in bone tissue repair and regeneration. Furthermore, OCN immunofluorescence staining (Fig. 7D) demonstrated that f-exo elevated the expression of OCN, an osteogenic differentiation-related protein. This suggests that f-exo was capable of promoting osteogenesis. Fig. 7G presents the quantitative analysis of the intensity of the three fluorescent stainings, thereby confirming the positive effect of f-exo in promoting osteogenic and angiogenic activities. In conclusion, the results demonstrate that f-exo possesses a distinctive capacity to address periprosthetic osteolysis in vivo by regulating bone metabolic homeostasis.

### 3.5. Potential mechanism of f-exo in targeting-regulation of bone metabolic homeostasis through proteomic analysis

To explore the potential mechanism of f-exo in the targeting-regulation of bone metabolic homeostasis, we performed proteomic analysis of M2-exo, USC-exo, and f-exo. The quality control results show that 4284 peptides were found in all samples, and most of the peptides contained 7–20 amino acids (Fig. S3A). The PCA diagram indicated good repeatability (Fig. S3B). There were 1096, 966, and 1083 proteins in the M2-exo, USC-exo and f-exo, respectively (Fig. S3C).

Gene Ontology (GO) analysis of three groups of detected proteins in the biological process (BP), and molecular function (MF) category revealed possible biological functions of these exosomes. These analyses suggest that f-exo carries a large number of proteins related to cell adhesion and integrins, which may be related to its mechanism of targeting osteolytic region; meanwhile, f-exo carries a large number of proteins related to the promotion of angiogenesis, cell migration, and the promotion of osteogenesis (Fig. 8A and B). The function of detected proteins was analyzed with the Kyoto Encyclopedia of Genes and Genomes (KEGG) pathway. The f-exo plays a role in the regulation of bone

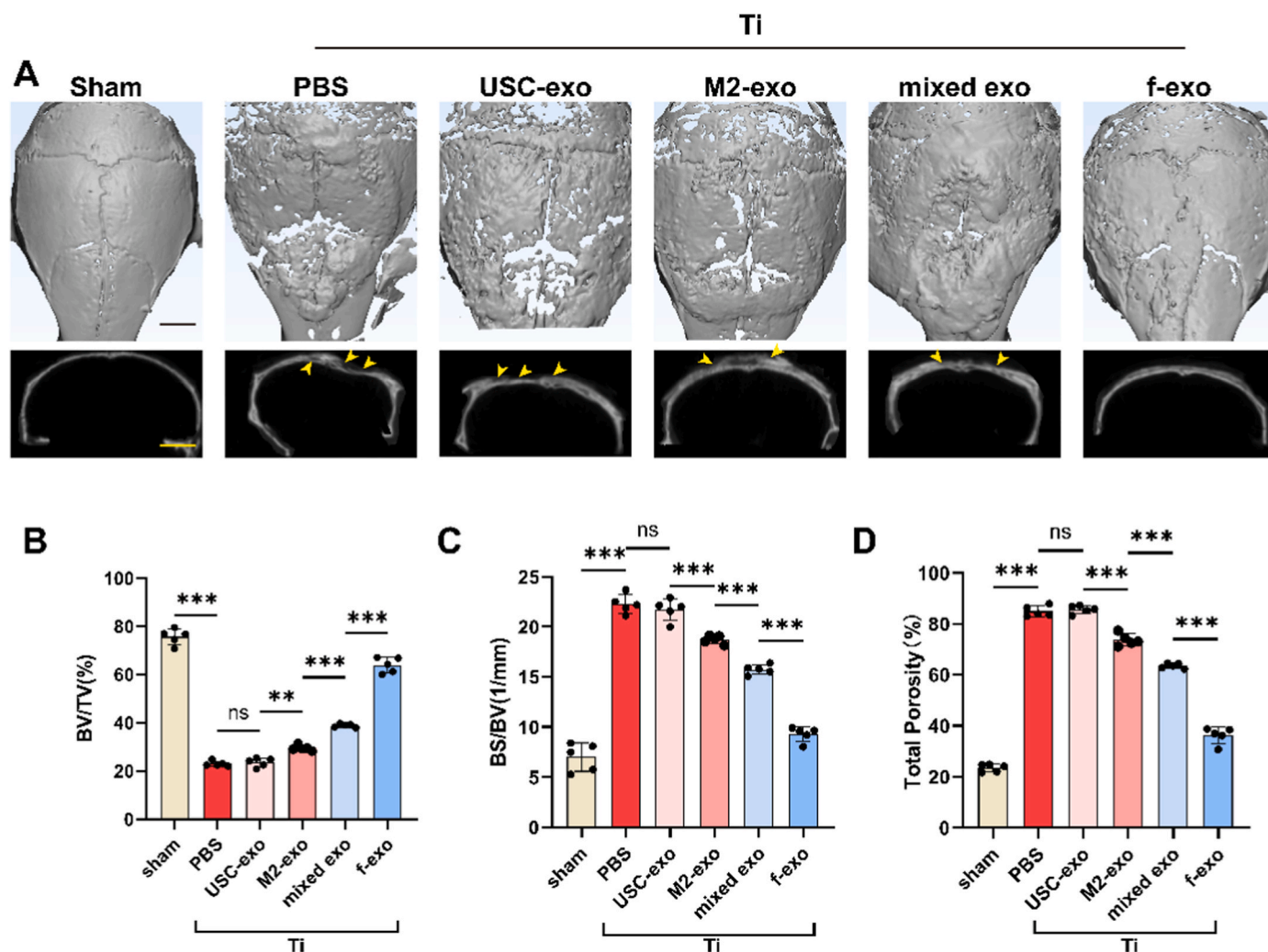


**Fig. 6.** Effect of f-exo against periprosthetic osteolysis in vivo (A) Representative micro-CT images of the erosion region of calvaria sections. Scale bar, 5 mm. (B, C, D) The quantitative analysis of BS/BV, BV/TV, and total porosity. (The data in the figures represent the averages  $\pm$  SD,  $n = 5$  samples per group,  $^*P < 0.05$ ,  $^{**}P < 0.01$ ,  $^{***}P < 0.001$ ).

metabolic homeostasis by modulating various metabolic functions and acting on different signaling pathways such as ECM receptor, HIF-1, and PI3K-Akt (Fig. 8C and D). Both GO and KEGG analysis reveal these proteins are all inherited from M2-exo, and USC-exo (Figure S4 A-C), which also validates the successful preparation of f-exo and f-exo retains the advantages of both two exosomes.

To explore the specific proteins involved in the targeted regulation of bone metabolic homeostasis, we analyzed the differential proteins of M2-exo and USC-exo. The volcano map shows a total of 467 differentially expressed proteins between the M2-exo and USC-exo two groups, of which 325 were highly expressed in M2-exo and 147 were enriched in USC-exo (Fig. 8E). Subsequently, the differential proteins were hierarchically clustered. These proteins are presented in an expression heatmap (Fig. 8F). Integrin, alpha M (ITGAM), and Integrin beta-2 (ITGB2) were high expressed in M2-exo versus USC-exo (Fig. 8E). ITGAM binds to ITGB2 to form integrin  $\alpha$ M $\beta$ 2 (Mac-1), a member of the classical  $\beta$ 2 integrin family, which plays an important role for M2-exo and f-exo in targeting the inflammatory endothelium and promoting mediated targeted adhesion mediated by transendothelial migration [34].

In the subsequent analysis, we applied Gene Set Enrichment Analysis (GSEA) to compare the protein expression between the M2-exo and USC-exo, which showed that M2-exo and USC-exo specific proteins were enriched in HIF-1 signal pathway (NES of  $-1.37$ ) (Fig. 8G). Several proteins highly expressed in M2-exo, such as alpha-enolase (ENO1),

epidermal growth factor receptor (EGFR), L-lactate dehydrogenase A chain (LDHA), L-lactate dehydrogenase B chain (LDHB), and several other proteins highly expressed in USC-exo, such as tissue factor (TF), plasminogen activator inhibitor 1 (SERPINE 1), fructose-bisphosphate aldolase B (ALDOB), promote angiogenesis by regulating the HIF-1 signaling pathway (Fig. 8H). Meanwhile, ATPase  $H^+$  transporting accessory protein 2 (SERPINE 1ATP6AP2), integrin-linked protein kinase (ILK), inactive tyrosine-protein kinase 7 (PTK7) and other proteins highly expressed in M2-exo and USC-exo inhibit osteoclast formation and promote osteogenesis by regulating the canonical Wnt signaling pathway (Fig. 8I).

Enrichment analysis showed that f-exo regulates osteogenic differentiation, osteoclast function, angiogenesis, and bone metabolic homeostasis through multiple pathways, providing a theoretical basis for the fulfillment of its biological functions.

#### 4. Discussion

Total joint arthroplasty (TJA) is the ultimate treatment for end-stage osteoarthritis. However, prosthetic-associated periprosthetic osteolysis mediated by wear particles and subsequent aseptic loosening of the prosthesis are the most severe complications associated with TJA [2]. Literature research indicates that bone metabolic disturbances around the prosthesis after TJA are the primary cause of eventual aseptic



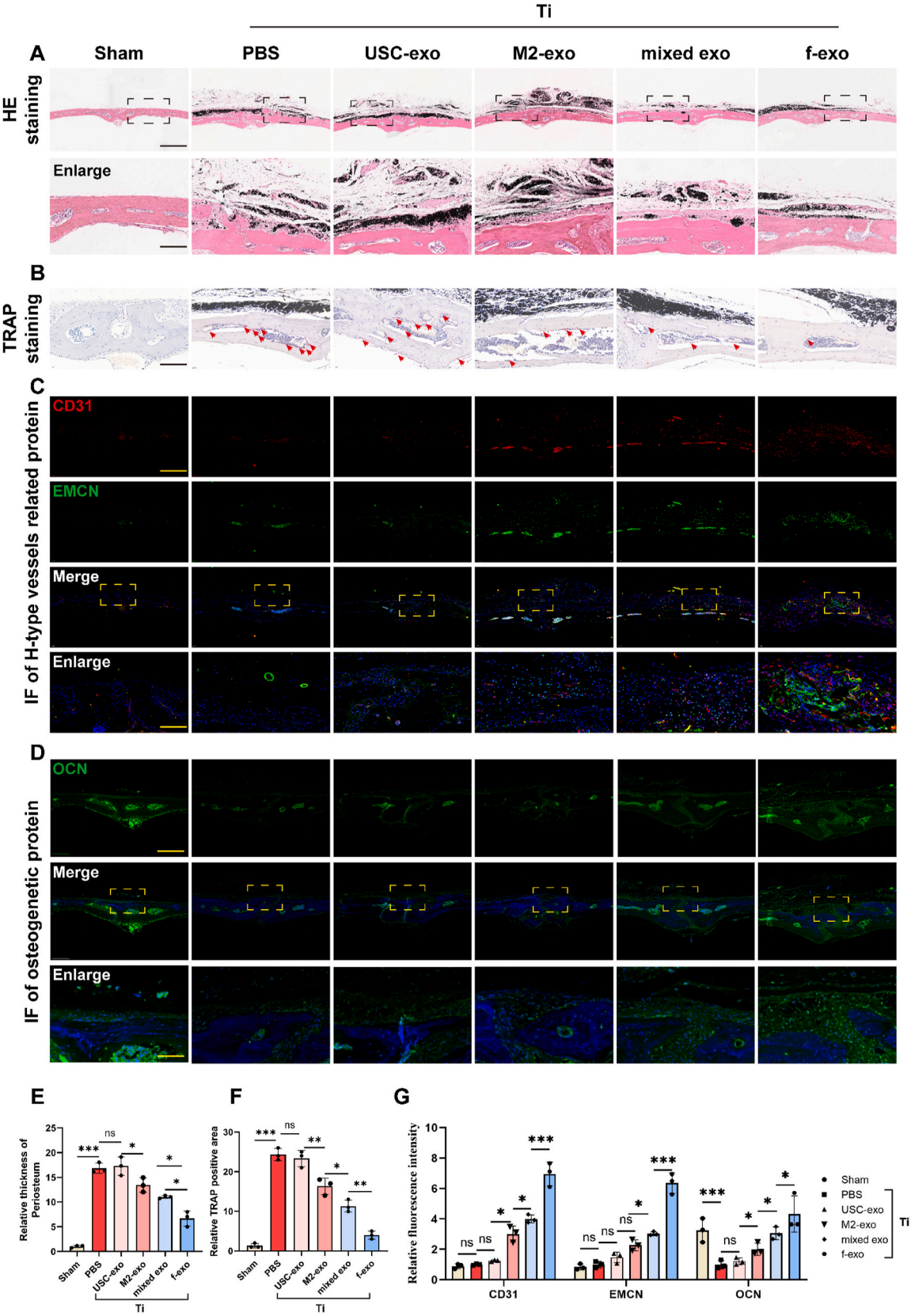


**Fig. 7.** Effect of f-exo against periprosthetic osteolysis in vivo (A) H&E staining of calvaria sections. Scale bar, 500  $\mu$ m, 150  $\mu$ m (enlarged). and TRAP staining (B) of calvaria sections. (TRAP positive cells were marked by red arrow) (E, F) Quantification of thickness of periosteum and TRAP positive area. (C, D) Typical immunofluorescence assay image of H-type vessels and osteogenesis related protein, and (G) their quantifications. Scale bar, 200  $\mu$ m, 50  $\mu$ m (enlarged) (The data in the figures represent the averages  $\pm$  SD, n = 3 samples per group, \* $P$  < 0.05, \*\* $P$  < 0.01, \*\*\* $P$  < 0.001).

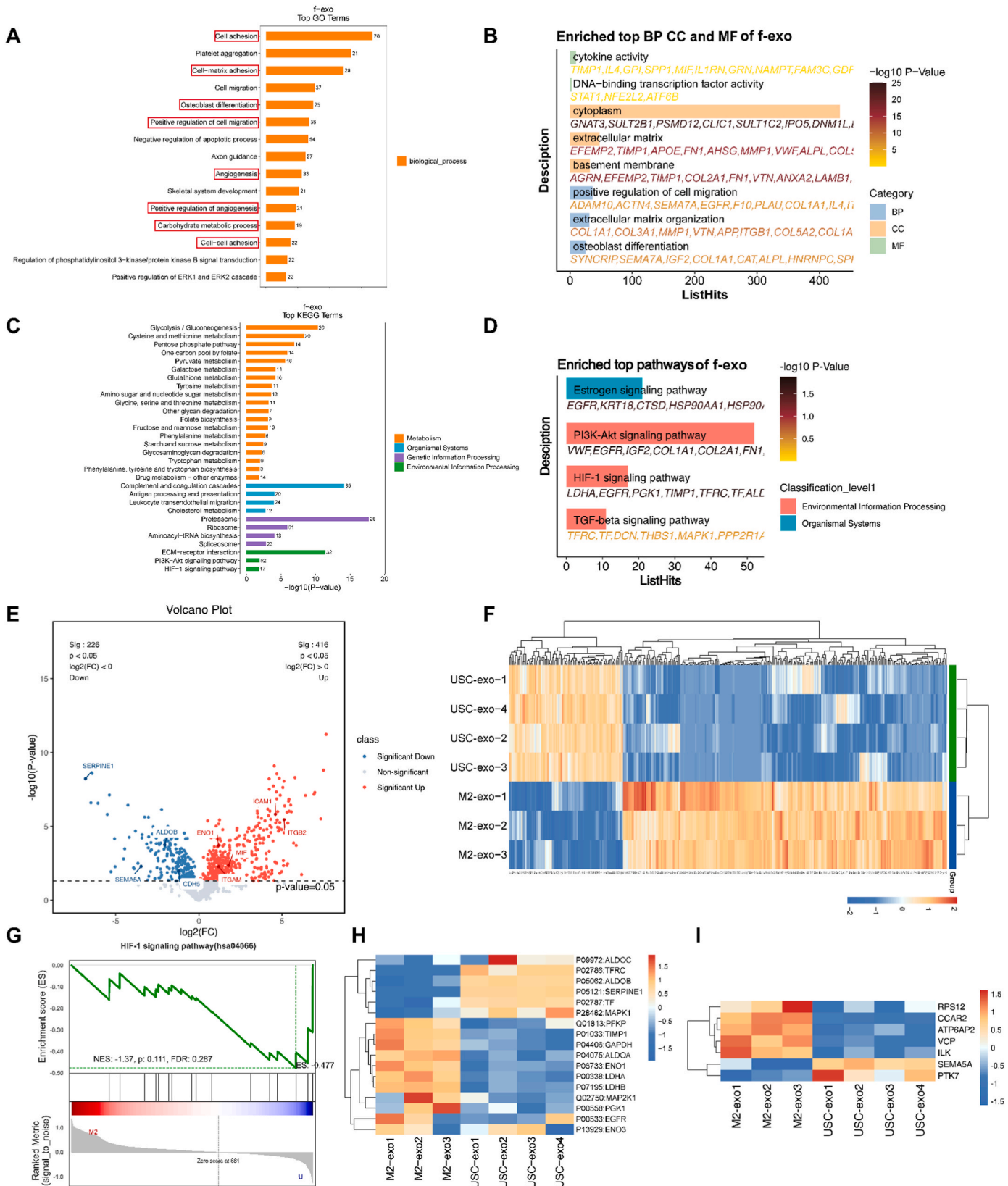


**Fig. 8.** Proteomic analysis of M2-exo, USC-exo and f-exo (A, B) GO enrichment analysis of proteins detected in f-exo. (C, D) KEGG enrichment analysis of proteins detected in f-exo. (E, F) Volcano gram and heat map of differential proteins for M2-exo versus USC-exo. (G) GSEA in HIF-1 signal pathway of differentially expressed protein in M2-exo and USC-exo. Differentially expressed protein in M2-exo and USC-exo in (H) HIF-1 signaling pathway and (G) canonical Wnt signaling pathway.



loosening, manifested by the activation of the RANK/RANKL/OPG signaling pathway, reduced osteogenesis and angiogenesis, and increased bone resorption [9,35,36]. Wear particles inhibit the functions of osteoblasts and endothelial cells through both phagocytic and non-phagocytic pathways [37,38]. The inflammatory environment induced by these particles promotes macrophage recruitment and osteoclast differentiation, ultimately leading to failure in the integration between the prosthesis and bone, as well as ischemic necrosis of the surrounding tissues [39–42]. To address these issues, the present study innovatively employs f-exo derived from M2-exo and USC-exo to target and regulate periprosthetic bone metabolic homeostasis after TJA. However, the successful fusion of f-exo faces challenges. Through a series of compelling experimental results, we demonstrated the efficient fusion of f-exo while preserving the composition and functionality of the constituent exosomes. The clinical application of f-exo offers significant advantages, enhancing targeting specificity, therapeutic efficacy, and biocompatibility through synergistic effects. While USC-exo possesses superior abilities in promoting angiogenesis, osteogenesis, and inhibiting bone resorption, it suffers from instability in systemic release and a lack of local targeting capacity around the prosthesis [22,43]. Studies have shown that M2-exo inherits surface components from macrophage membranes, endowing it with enhanced inflammation-targeting and immune evasion capabilities [44]. Additionally, M2-exo plays a role in bone metabolic homeostasis by promoting osteogenesis, angiogenesis, and inhibiting bone resorption [25,27,45]. Based on these findings, we successfully constructed f-exo using exosome fusion technology, enabling it to specifically target the inflammatory region around the prosthesis while simultaneously exerting the synergistic therapeutic effects of both exosome types.

The f-exo constructed via exosome fusion technology retains the therapeutic components of both M2-exo and USC-exo, thus possessing the ability to target and regulate periprosthetic bone metabolic homeostasis. MicroRNAs (miRNAs) are small endogenous RNAs that can regulate the expression of target genes through various mechanisms [46]. Previous studies have shown that USC-exo can enrich miR-26a-5p, which inhibits HDAC4, thereby activating the HIF-1 $\alpha$ /VEGFA pathway to enhance osteoblast activity [47]. Moreover, USC-exo promotes osteogenesis and inhibits bone resorption by transferring collagen triple-helix repeat containing 1 (CTHRC1) and osteoprotegerin (OPG) [20]. The highly expressed miR-21-5p, miR-30, and miR-148a-3p in USC-exo collectively promote angiogenesis [47,48]. M2-exo also plays a role in regulating bone metabolic homeostasis. M2-exo promotes angiogenesis following myocardial infarction by downregulating the expression of THBS1 mRNA via miR-132-3p [49]. Furthermore, M2-exo delivers miR-486-5p and miR-26a-5p to induce osteogenic differentiation of BMSCs [50,51]. Additionally, M2-exo transfers IL-10 mRNA to macrophages, activating the IL-10/IL-10R pathway to inhibit osteoclast differentiation [27]. In our study, the proteomic analysis revealed multiple proteins such as SERPINE 1, and ATP6AP2 that are specifically expressed in M2-exo and USC-exo to achieve enhanced osteogenesis, angiogenesis, and inhibition of osteoclastogenesis through HIF-1, Wnt, and other signaling pathways to regulate bone metabolic homeostasis [52–55]. These findings highlight the potential mechanisms by which f-exo regulates periprosthetic bone metabolic homeostasis.

The dual effects of f-exo, derived [55] from both M2-exo and USC-exo, in vivo are closely related to its targeting ability at the prosthetic site. Natural cell membranes possess various functions associated with their source cells, including "self" recognition, biological targeting, and interaction with the immune system [56]. Nanoparticles encapsulated in cell membranes exhibit specific biological functions, such as prolonged circulation time, target recognition, enhanced accumulation at disease sites, and deeper penetration into tumors [57]. Co-extrusion is the most commonly used method for preparing fusion vesicles, where mechanical forces from a mini-extruder generate uniform hybrid vesicles from membrane components of different cellular origins [58]. Co-extrusion of platelet membrane vesicles (PMV) and mesenchymal

stem cell exosomes (MSC-Exos) not only preserves the natural ability of platelets to target cardiac injury, but also inherits the function of mesenchymal stem cells in repairing vascular damage and promoting angiogenesis [59]. The role of inflammation in periprosthetic osteolysis cannot be overlooked. Previous studies have shown that M2-exo can effectively target inflammatory sites as a drug delivery vehicle [44,60], and the inflammatory microenvironment induced by wear particles after joint arthroplasty may facilitate the local targeting and accumulation of M2-exo around the prosthesis [61]. On the other hand, the specific surface markers of M2-exo accumulate selectively in the inflammatory region via receptor-mediated mechanisms. These markers include cell membrane-associated proteins such as P-selectin glycoprotein ligand 1 (PSGL-1), L-selectin, lymphocyte function-associated antigen 1 (LFA-1), integrins, and very late antigen 4 (VLA-4) [57]. In our study, the targeting of f-exo to the periprosthetic osteolytic region is attributed to the macrophage membrane components from M2-exo. During the fusion process, the surface proteins from M2-exo are embedded into the USC-exo membrane structure through self-assembly, and the strong affinity between the surface proteins and the exosomal membrane ensures their retention on the surface of the fused complex. ITGAM and ITGB2 were highly expressed in M2-exo in the proteomic analysis. ITGAM binds to ITGB2 to form the integrin  $\alpha$ M $\beta$ 2 (Mac-1), a member of the classical  $\beta$ 2 integrin family. The integrin  $\alpha$ M $\beta$ 2 mediates the specific binding of exosomes to the inflamed endothelium by recognizing ICAM-1 (intercellular adhesion molecule-1) or VCAM-1 (vascular cell adhesion molecule-1) on the endothelial cell surface. By decreasing VE-cadherin and ZO-1 expression in inflammatory endothelial cells, and increasing ICAM-1 expression, the ITGAM and ITGB2 high expressed exosomes enhance the ability of exosomes to penetrate the vascular barrier to target the inflammatory region [34]. Therefore, the targeting effect of M2-exo is not only dependent on the inflammatory response around the prosthesis but may also be related to the targeting properties of its surface markers.

Based on the structural foundation of the phospholipid bilayer of exosomal membranes, we successfully constructed f-exo by using exosome fusion technology, combining M2-exo with USC-exo for the first time. This fused exosome system achieved targeted regulation of periprosthetic bone metabolic homeostasis and therapeutic effects on periprosthetic osteolysis after joint arthroplasty [62]. The f-exo system provides an innovative therapeutic strategy, with high targeting specificity, low toxicity, and long-lasting effects, offering distinct advantages over traditional therapies: (1) By fusing M2-exo and USC-exo, f-exo can precisely target the osteolytic regions surrounding the prosthesis and implement local therapy via receptor-mediated mechanisms, significantly reducing systemic side effects. (2) The dual therapeutic effects of M2-exo and USC-exo in f-exo can effectively inhibit osteoclast activity while promoting angiogenesis and bone repair, providing a more comprehensive therapeutic outcome. (3) f-exo demonstrates good biocompatibility and stability, enabling prolonged activity in vivo, thus providing sustained therapeutic effects. Although our study has yielded a series of original findings, it still has certain limitations: (1) Long-term exosome-based therapy may provoke immune responses, and prolonged retention in the body may lead to potential accumulation effects or chronic inflammatory reactions [63]. (2) The production and purification processes of exosomes are relatively complex, and costly, and may face batch-to-batch variations during large-scale production, which could lead to off-target effects and compromise therapeutic outcomes [46]. (3) Our study utilized cells from different species, which may result in differences in immune responses, cellular signaling pathways, metabolic mechanisms, and exosome uptake processes. (4) We used standard in vitro cell models to preliminarily validate the potential effects of exosome-based therapy on periprosthetic osteolysis, but did not fully replicate the aseptic inflammatory microenvironment induced by wear particles. (5) The shear stress generated during the co-extrusion process may compromise the integrity of the natural exosomal membrane [64]. The combination of multiple vesicle fusion techniques, such

as freeze-thawing [65] and polyethylene glycol (PEG) induction [66], for preparing and assessing f-exo fusion efficiency remains to be further explored. (6) We applied proteomic analysis of exosome to explore the biological function, but the role of miRNA in exocytosis has not been the focus of attention. In response to these limitations, we propose targeted solutions and future research directions: (1) Standardizing exosome isolation methods, establishing rigorous production standards, and developing long-term efficacy evaluation systems. (2) Isolating and fusing exosomes derived from autologous cells, and surface-modifying exosomes to enhance delivery efficiency while reducing immunogenicity. (3) Employing genetic engineering and introducing specific targeting ligands to further improve the targeting specificity and biocompatibility of exosomes [67]. (4) Combined multi-omics analysis of exosomes' components was used to investigate their specific biological mechanisms [55]. These research directions will provide a solid foundation for the clinical translation of exosome-based therapies.

Effectively preventing and treating periprosthetic osteolysis remains a long-term management challenge after joint arthroplasty. The f-exo derived from autologous cells offers a novel approach to targeting the periprosthetic region and effectively regulating bone metabolic homeostasis, providing a new strategy for preventing periprosthetic osteolysis [68]. In terms of clinical feasibility, the preparation of f-exo has been successfully achieved in laboratory settings, and exosome preparation technology has already been applied in clinical research. Therefore, we believe it is feasible to translate this technology into clinical applications. Although there are still challenges in large-scale production and standardization, we are confident that with advancements in technology and optimization of the processes, f-exo will be capable of large-scale production to meet clinical needs in the future. However, there are still several challenges to the clinical application of f-exo. First, the exosome preparation process needs further optimization to ensure consistency and quality in large-scale production [46]. Secondly, optimization of targeting and in vivo distribution remains an important research direction. Future studies will need to further evaluate its efficacy in various disease models and assess its safety and effectiveness through preclinical animal studies and clinical trials. To successfully apply f-exo in clinical settings, further validation in animal models, standardized production, quality control, clinical trial planning and implementation, long-term follow-up, and optimization through multidisciplinary cooperation and regulatory review are necessary. The effective integration of f-exo with other orthopedic treatments or technologies could offer more comprehensive therapeutic solutions, such as synergistic effects with drug therapies, integration with physical therapy, combination with gene therapy, and collaboration with biomaterials and bioprinting technologies. In the future of regenerative medicine, especially in orthopedic applications, f-exo-based therapies undoubtedly have immense potential. f-exo can effectively carry various bioactive molecules, such as RNA, proteins, and lipids, and precisely target damaged tissues, offering more personalized treatment options. In our study, f-exo primarily focuses on periprosthetic osteolysis, but we believe this finding can also make significant contributions to other areas of drug-targeted delivery systems. Fused exosomes derived from different exosome sources could provide new clinical therapeutic strategies for a range of diseases, including cancer treatment, immune modulation, neurodegenerative diseases, cardiovascular diseases, and diabetes.

#### CRediT authorship contribution statement

**Tianliang Ma:** Writing – review & editing, Methodology. **Qimeng Liu:** Writing – original draft, Methodology, Conceptualization. **Zheyu Zhang:** Software, Methodology. **Jiangyu Nan:** Methodology, Investigation. **Guanzhi Liu:** Software, Data curation. **Yute Yang:** Software, Funding acquisition, Data curation. **Yihe Hu:** Writing – review & editing, Supervision, Funding acquisition. **Jie Xie:** Writing – review & editing, Supervision, Funding acquisition.

#### Data availability statement

The data underlying this study will be shared on reasonable request to the corresponding author.

#### Ethics approval and consent to participate

The collection of urine samples and their use for scientific research was approved by Clinical Research Ethics Committee of the First Affiliated Hospital of Zhejiang University School of Medicine (No. 11T20230385B-R1). Animal experimentation procedures adhered strictly to protocols approved by the Experimental Animal Ethics Committee of the First Affiliated Hospital of Zhejiang University School of Medicine (2023 No. 1394), and all experimental animals were kept under SPF conditions during the experiments.

#### Declaration of competing interest

The authors declare no conflict of interest.

#### Acknowledgments

This work was supported by the Zhejiang Provincial Natural Science Foundation of China under grant number LQN25H060009 and Y24H060021 and the National Natural Science Foundation of China under grant numbers 82372414, 82272452 and 82202733. Graph abstract was created with [BioRender.com](https://www.biorender.com). The authors extend their gratitude to Ms. Ma from Shiyanjia Lab ([www.shiyanjia.com](http://www.shiyanjia.com)) for providing invaluable assistance with the TEM and OE Biotech Co., Ltd (Shanghai, China) for providing proteomic analysis.

#### Appendix A. Supplementary data

Supplementary data to this article can be found online at <https://doi.org/10.1016/j.bioactmat.2025.04.006>.

#### References

- [1] Y. Xie, Y. Peng, G. Fu, J. Jin, S. Wang, M. Li, Q. Zheng, F.J. Lyu, Z. Deng, Y. Ma, Nano wear particles and the periprosthetic microenvironment in aseptic loosening induced osteolysis following joint arthroplasty, *Front. Cell. Infect. Microbiol.* 13 (2023) 1275086.
- [2] S.B. Goodman, J. Gallo, Periprosthetic osteolysis: mechanisms, prevention and treatment, *J. Clin. Med.* 8 (12) (2019).
- [3] B. Pan, Z. Zhang, X. Wu, G. Xian, X. Hu, M. Gu, L. Zheng, X. Li, L. Long, W. Chen, P. Sheng, Macrophage-derived exosomes modulate wear particle-induced osteolysis via miR-3470b targeting TAB3/NF- $\kappa$ B signaling, *Bioact. Mater.* 26 (2023) 181–193.
- [4] Q. Wang, W. Zhang, X. Peng, Y. Tao, Y. Gu, W. Li, X. Liang, L. Wang, Z. Wu, T. Wang, H. Zhang, X. Liu, Y. Xu, Y. Liu, J. Zhou, D. Geng, GSK-3 $\beta$  suppression upregulates Gli1 to alleviate osteogenesis inhibition in titanium nanoparticle-induced osteolysis, *J. Nanobiotechnol.* 20 (1) (2022) 148.
- [5] N. Cobelli, B. Scharf, G.M. Crisi, J. Hardin, L. Santambrogio, Mediators of the inflammatory response to joint replacement devices, *Nat. Rev. Rheumatol.* 7 (10) (2011) 600–608.
- [6] H. Alhasan, M.A. Terkawi, G. Matsumae, T. Ebata, Y. Tian, T. Shimizu, Y. Nishida, S. Yokota, F. Garcia-Martin, M.A.E. M., D. Takahashi, M.A. Younis, H. Harashima, K. Kadoya, N. Iwasaki, Inhibitory role of Annexin A1 in pathological bone resorption and therapeutic implications in periprosthetic osteolysis, *Nat. Commun.* 13 (1) (2022) 3919.
- [7] R. Florencio-Silva, G.R. Sasso, E. Sasso-Cerri, M.J. Simões, P.S. Cerri, Biology of bone tissue: structure, function, and factors that influence bone cells, *BioMed Res. Int.* 2015 (2015) 421746.
- [8] N.A. Sims, J.H. Gooi, Bone remodeling: multiple cellular interactions required for coupling of bone formation and resorption, *Semin. Cell Dev. Biol.* 19 (5) (2008) 444–451.
- [9] H. Xie, Z. Cui, L. Wang, Z. Xia, Y. Hu, L. Xian, C. Li, L. Xie, J. Crane, M. Wan, G. Zhen, Q. Bian, B. Yu, W. Chang, T. Qiu, M. Pickarski, L.T. Duong, J.J. Windle, X. Luo, E. Liao, X. Cao, PDGF-BB secreted by preosteoclasts induces angiogenesis during coupling with osteogenesis, *Nat. Med.* 20 (11) (2014) 1270–1278.
- [10] S.M. Chim, J. Tickner, S.T. Chow, V. Kuek, B. Guo, G. Zhang, V. Rosen, W. Erber, J. Xu, Angiogenic factors in bone local environment, *Cytokine Growth Factor Rev.* 24 (3) (2013) 297–310.

- [11] M.L. Brandi, P. Collin-Osdoby, Vascular biology and the skeleton, *J. Bone Miner. Res.* 21 (2) (2006) 183–192.
- [12] K. Matsuo, N. Irie, Osteoclast-osteoblast communication, *Arch. Biochem. Biophys.* 473 (2) (2008) 201–209.
- [13] J.M. Kim, C. Lin, Z. Stavre, M.B. Greenblatt, J.H. Shim, Osteoblast-osteoclast communication and bone homeostasis, *Cells* 9 (9) (2020).
- [14] N. Udagawa, M. Koide, M. Nakamura, Y. Nakamichi, T. Yamashita, S. Uehara, Y. Kobayashi, Y. Furuu, H. Yasuda, C. Fukuda, E. Tada, Osteoclast differentiation by RANKL and OPG signaling pathways, *J. Bone Miner. Metabol.* 39 (1) (2021) 19–26.
- [15] S. Theoleyre, Y. Wittrant, S.K. Tat, Y. Fortin, F. Redini, D. Heymann, The molecular triad OPG/RANK/RANKL: involvement in the orchestration of pathophysiological bone remodeling, *Cytokine Growth Factor Rev.* 15 (6) (2004) 457–475.
- [16] X. Li, J. Liao, X. Su, W. Li, Z. Bi, J. Wang, Q. Su, H. Huang, Y. Wei, Y. Gao, J. Li, L. Li, C. Wang, Human urine-derived stem cells protect against renal ischemia/reperfusion injury in a rat model via exosomal which targets, *Theranostics* 10 (21) (2020) 9561–9578.
- [17] C.Y. Chen, W. Du, S.S. Rao, Y.J. Tan, X.K. Hu, M.J. Luo, Q.F. Ou, P.F. Wu, L. M. Qing, Z.M. Cao, H. Yin, T. Yue, C.H. Zhan, J. Huang, Y. Zhang, Y.W. Liu, Z. X. Wang, Z.Z. Liu, J. Cao, J.H. Liu, C.G. Hong, Z.H. He, J.X. Yang, S.Y. Tang, J. Y. Tang, H. Xie, Extracellular vesicles from human urine-derived stem cells inhibit glucocorticoid-induced osteonecrosis of the femoral head by transporting and releasing pro-angiogenic DMBT1 and anti-apoptotic TIMP1, *Acta Biomater.* 111 (2020) 208–220.
- [18] Q. Zhu, Q. Li, X. Niu, G. Zhang, X. Ling, J. Zhang, Y. Wang, Z. Deng, Extracellular vesicles secreted by human urine-derived stem cells promote ischemia repair in a mouse model of hind-limb ischemia, *Cell. Physiol. Biochem.* 47 (3) (2018) 1181–1192.
- [19] C.Y. Chen, S.S. Rao, L. Ren, X.K. Hu, Y.J. Tan, Y. Hu, J. Luo, Y.W. Liu, H. Yin, J. Huang, J. Cao, Z.X. Wang, Z.Z. Liu, H.M. Liu, S.Y. Tang, R. Xu, H. Xie, Exosomal DMBT1 from human urine-derived stem cells facilitates diabetic wound repair by promoting angiogenesis, *Theranostics* 8 (6) (2018) 1607–1623.
- [20] C.Y. Chen, S.S. Rao, Y.J. Tan, M.J. Luo, X.K. Hu, H. Yin, J. Huang, Y. Hu, Z.W. Luo, Z.Z. Liu, Z.X. Wang, J. Cao, Y.W. Liu, H.M. Li, Y. Chen, W. Du, J.H. Liu, Y. Zhang, T.H. Chen, H.M. Liu, B. Wu, T. Yue, Y.Y. Wang, K. Xia, P.F. Lei, S.Y. Tang, H. Xie, Extracellular vesicles from human urine-derived stem cells prevent osteoporosis by transferring CTHRC1 and OPG, *Bone Res* 7 (2019) 18.
- [21] Y.Z. Huang, T. He, J. Cui, Y.L. Jiang, J.F. Zeng, W.Q. Zhang, H.Q. Xie, Urine-derived stem cells for regenerative medicine: basic biology, applications, and challenges, *Tissue Eng., Part B* 28 (5) (2022) 978–994.
- [22] C. He, S. Zheng, Y. Luo, B. Wang, Exosome theranostics: biology and translational medicine, *Theranostics* 8 (1) (2018) 237–255.
- [23] S. Rayamajhi, T.D.T. Nguyen, R. Marasini, S. Aryal, Macrophage-derived exosome-mimetic hybrid vesicles for tumor targeted drug delivery, *Acta Biomater.* 94 (2019) 482–494.
- [24] Y. Zhang, K. Cai, C. Li, Q. Guo, Q. Chen, X. He, L. Liu, Y. Zhang, Y. Lu, X. Chen, T. Sun, Y. Huang, J. Cheng, C. Jiang, Macrophage-membrane-coated nanoparticles for tumor-targeted chemotherapy, *Nano Lett.* 18 (3) (2018) 1908–1915.
- [25] Y. Yang, Z. Guo, W. Chen, X. Wang, M. Cao, X. Han, K. Zhang, B. Teng, J. Cao, W. Wu, P. Cao, C. Huang, Z. Qiu, M2 macrophage-derived exosomes promote angiogenesis and growth of pancreatic ductal adenocarcinoma by targeting E2F2, *Mol. Ther.* 29 (3) (2021) 1226–1238.
- [26] C. Hou, Y. Zhang, Z. Lv, Y. Luan, J. Li, C. Meng, K. Liu, X. Luo, L. Chen, F. Liu, Macrophage exosomes modified by miR-365-2-5p promoted osteoblast osteogenic differentiation by targeting OLFML1, *Regen. Biomater.* 11 (2024) rbae018.
- [27] X. Chen, Z. Wan, L. Yang, S. Song, Z. Fu, K. Tang, L. Chen, Y. Song, Exosomes derived from reparative M2-like macrophages prevent bone loss in murine periodontitis models via IL-10 mRNA, *J. Nanobiotechnol.* 20 (1) (2022) 110.
- [28] Y. Zou, Y. Sun, Y. Wang, D. Zhang, H. Yang, X. Wang, M. Zheng, B. Shi, Cancer cell-mitochondria hybrid membrane coated Gboxin loaded nanomedicines for glioblastoma treatment, *Nat. Commun.* 14 (1) (2023) 4557.
- [29] Y. Jiang, M. Yu, Z.F. Song, Z.Y. Wei, J. Huang, H.Y. Qian, Targeted delivery of mesenchymal stem cell-derived bioinspired exosome-mimetic nanovesicles with platelet membrane fusion for atherosclerotic treatment, *Int. J. Nanomed.* 19 (2024) 2553–2571.
- [30] S. Jiang, G. Cai, Z. Yang, H. Shi, H. Zeng, Q. Ye, Z. Hu, Z. Wang, Biomimetic nanovesicles as a dual gene delivery system for the synergistic gene therapy of alzheimer's disease, *ACS Nano* 18 (18) (2024) 11753–11768.
- [31] J. Xie, Y. Hu, H. Li, Y. Wang, X. Fan, W. Lu, R. Liao, H. Wang, Y. Cheng, Y. Yang, J. Wang, S. Liang, T. Ma, W. Su, Targeted therapy for peri-prosthetic osteolysis using macrophage membrane-encapsulated human urine-derived stem cell extracellular vesicles, *Acta Biomater.* 160 (2023) 297–310.
- [32] L.C.A. Stiekema, L. Willemsen, Y. Kaiser, K.H.M. Prange, N.J. Wareham, S. M. Boekholdt, C. Kuijk, M.P.J. de Winther, C. Voermans, M. Nahrendorf, E.S. G. Strokes, J. Kroon, Impact of cholesterol on proinflammatory monocyte production by the bone marrow, *Eur. Heart J.* 42 (42) (2021) 4309–4320.
- [33] F. Liu, Y. Yuan, L. Bai, L. Yuan, L. Li, J. Liu, Y. Chen, Y. Lu, J. Cheng, J. Zhang, LRRc17 controls BMSC senescence via mitophagy and inhibits the therapeutic effect of BMSCs on ovariectomy-induced bone loss, *Redox Biol.* 43 (2021) 101963.
- [34] Q. Hu, S. Zhang, Y. Yang, J. Li, H.X. Kang, W.F. Tang, C.J. Lyon, M.H. Wan, Extracellular vesicle ITGAM and ITGB2 mediate severe acute pancreatitis-related acute lung injury, *ACS Nano* 17 (8) (2023) 7562–7575.
- [35] S.C. O'Neill, J.M. Queally, B.M. Devitt, P.P. Doran, J.M. O'Byrne, The role of osteoblasts in peri-prosthetic osteolysis, *Bone Joint Lett.* J 95-B (8) (2013) 1022–1026.
- [36] Z. Yin, G. Gong, X. Liu, J. Yin, Mechanism of regulating macrophages/osteoclasts in attenuating wear particle-induced aseptic osteolysis, *Front. Immunol.* 14 (2023) 1274679.
- [37] C. Vermes, R. Chandrasekaran, J.J. Jacobs, J.O. Galante, K.A. Roebuck, T.T. Glant, The effects of particulate wear debris, cytokines, and growth factors on the functions of MG-63 osteoblasts, *J. Bone Joint Surg Am* 83 (2) (2001) 201–211.
- [38] E.A. Fritz, T.T. Glant, C. Vermes, J.J. Jacobs, K.A. Roebuck, Chemokine gene activation in human bone marrow-derived osteoblasts following exposure to particulate wear debris, *J. Biomed. Mater. Res.* 77 (1) (2006) 192–201.
- [39] K. Lochner, A. Fritsche, A. Jonitz, D. Hansmann, P. Mueller, B. Mueller-Hilke, R. Bader, The potential role of human osteoblasts for periprosthetic osteolysis following exposure to wear particles, *Int. J. Mol. Med.* 28 (6) (2011) 1055–1063.
- [40] C.C. Okafor, H. Haleem-Smith, P. Laqueriere, P.A. Manner, R.S. Tuan, Particulate endocytosis mediates biological responses of human mesenchymal stem cells to titanium wear debris, *J. Orthop. Res.* 24 (3) (2006) 461–473.
- [41] J.M. Queally, B.M. Devitt, J.S. Butler, A.P. Malizia, D. Murray, P.P. Doran, J. M. O'Byrne, Cobalt ions induce chemokine secretion in primary human osteoblasts, *J. Orthop. Res.* 27 (7) (2009) 855–864.
- [42] S.B. Goodman, E. Gibon, J. Gallo, M. Takagi, Macrophage polarization and the osteoimmunology of periprosthetic osteolysis, *Curr. Osteoporos. Rep.* 20 (1) (2022) 43–52.
- [43] Y.J. Dong, J.J. Hu, Y.T. Song, Y.Y. Gao, M.J. Zheng, C.Y. Zou, M. Xiong, J. Li-Ling, H. Yang, H.Q. Xie, Extracellular vesicles from urine-derived stem cell for tissue engineering and regenerative medicine, *Tissue Eng., Part B* 30 (2) (2024) 176–197.
- [44] Z.S. Gao, C.J. Zhang, N. Xia, H. Tian, D.Y. Li, J.Q. Lin, X.F. Mei, C. Wu, Berberine-loaded M2 macrophage-derived exosomes for spinal cord injury therapy, *Acta Biomater.* 126 (2021) 211–223.
- [45] A. Daneshvar, P. Nemati, A. Azadi, R. Amid, M. Kakhodazadeh, M2 macrophage-derived exosomes for bone regeneration: a systematic review, *Arch. Oral Biol.* 166 (2024) 106034.
- [46] R. Kalluri, V.S. LeBleu, The biology, function, and biomedical applications of exosomes, *Science* 367 (6478) (2020).
- [47] D. Zhang, J. Du, M. Yu, L. Luo, Urine-derived stem cells-extracellular vesicles ameliorate diabetic osteoporosis through HDAC4/HIF-1 $\alpha$ /VEGFA axis by delivering microRNA-26a-5p, *Cell Biol. Toxicol.* 39 (5) (2022) 2243–2257.
- [48] B. Ouyang, Y. Xie, C. Zhang, C. Deng, L. Lv, J. Yao, Y. Zhang, G. Liu, J. Deng, C. Deng, Extracellular vesicles from human urine-derived stem cells ameliorate erectile dysfunction in a diabetic rat model by delivering proangiogenic MicroRNA, *Sex. Med.* 7 (2) (2019) 241–250.
- [49] H. Guo, Z. Li, B. Xiao, R. Huang, M2 macrophage-derived exosomes promote angiogenesis and improve cardiac function after myocardial infarction, *Biol. Direct* 19 (1) (2024) 43.
- [50] Z. Bin-Bin, Z.X. Da-Wa, L. Chao, Z. Lan-Tao, W. Tao, L. Chuan, L. Chao-Zheng, L. De-Chun, F. Chang, W. Shu-Qing, D. Zu-Nan, P. Xian-Wei, Z.X. Zhang, L. Ke-Wen, M2 macrophage-derived exosomal miRNA-26a-5p induces osteogenic differentiation of bone mesenchymal stem cells, *J. Orthop. Surg. Res.* 17 (1) (2022) 137.
- [51] J. Liu, Z. Sun, Y. You, L. Zhang, D. Hou, G. Gu, Y. Chen, G. Jiao, M2 macrophage-derived exosomal miR-486-5p influences the differentiation potential of bone marrow mesenchymal stem cells and osteoporosis, *Aging (Albany NY)* 15 (18) (2023) 9499–9520.
- [52] L. Xiong, H.H. Guo, J.X. Pan, X. Ren, D. Lee, L. Chen, L. Mei, W.C. Xiong, ATP6AP2, a regulator of LRP6/ $\beta$ -catenin protein trafficking, promotes Wnt/ $\beta$ -catenin signaling and bone formation in a cell type dependent manner, *Bone Research* 12 (1) (2024).
- [53] F. Santiago, J. Oguma, A.M.C. Brown, J. Laurence, Noncanonical Wnt signaling promotes osteoclast differentiation and is facilitated by the human immunodeficiency virus protease inhibitor ritonavir, *Biochem. Biophys. Res. Commun.* 417 (1) (2012) 223–230.
- [54] L.Y. Li, A.F. Li, L. Zhu, L.Y. Gan, L. Zuo, Roxadustat promotes osteoblast differentiation and prevents estrogen deficiency-induced bone loss by stabilizing HIF-1 $\alpha$  and activating the Wnt/ $\beta$ -catenin signaling pathway, *J. Orthop. Surg. Res.* 17 (1) (2022).
- [55] K.M. Talasila, A. Soentgerath, P. Euskirchen, G.V. Rosland, J. Wang, P.C. Huszthy, L. Prestegard, K.O. Skafnesmo, P.O. Sakariassen, E. Eskilsson, D. Stieber, O. Keunen, J. Nigro, O.K. Vintermyr, M. Lund-Johansen, S.P. Niclous, S. Smark, P. O. Enger, R. Bjerkvig, H. Miletic, Egrf wild-type amplification and activation promote invasion and development of glioblastoma independent of angiogenesis, *Neuro Oncol.* 15 (2013), 6–6.
- [56] H. Wang, J. Wu, G.R. Williams, Q. Fan, S. Niu, J. Wu, X. Xie, L.M. Zhu, Platelet-membrane-biomimetic nanoparticles for targeted antitumor drug delivery, *J. Nanobiotechnol.* 17 (1) (2019) 60.
- [57] Y. Wu, S. Wan, S. Yang, H. Hu, C. Zhang, J. Lai, J. Zhou, W. Chen, X. Tang, J. Luo, X. Zhou, L. Yu, L. Wang, A. Wu, Q. Fan, J. Wu, Macrophage cell membrane-based nanoparticles: a new promising biomimetic platform for targeted delivery and treatment, *J. Nanobiotechnol.* 20 (1) (2022) 542.
- [58] M. Sun, J. Yang, Y. Fan, Y. Zhang, J. Sun, M. Hu, K. Sun, J. Zhang, Beyond extracellular vesicles: hybrid membrane nanovesicles as emerging advanced tools for biomedical applications, *Adv. Sci. (Weinh.)* 10 (32) (2023) e2303617.
- [59] Q. Li, Y. Song, Q. Wang, J. Chen, J. Gao, H. Tan, S. Li, Y. Wu, H. Yang, H. Huang, Y. Yu, Y. Li, N. Zhang, Z. Huang, Z. Pang, J. Qian, J. Ge, Engineering extracellular vesicles with platelet membranes fusion enhanced targeted therapeutic angiogenesis in a mouse model of myocardial ischemia reperfusion, *Theranostics* 11 (8) (2021) 3916–3931.
- [60] T. Ma, S. Chen, J. Wang, S. Liang, M. Chen, Q. Liu, Z. Zhang, G. Liu, Y. Yang, Y. Hu, J. Xie, Enhanced osteolysis targeted therapy through fusion of exosomes derived

- from M2 macrophages and bone marrow mesenchymal stem cells: modulating macrophage polarization, *Small* 20 (7) (2024) e2303506.
- [61] I. Panez-Toro, D. Heymann, F. Gouin, J. Amiaud, M.F. Heymann, L.A. Cordova, Roles of inflammatory cell infiltrate in periprosthetic osteolysis, *Front. Immunol.* 14 (2023) 1310262.
- [62] X. Feng, A. Shen, W. Zhang, S. Jia, A. Iliuk, Y. Wang, W. Zhang, Y. Zhang, W. A. Tao, L. Hu, High-throughput capture and in situ protein analysis of extracellular vesicles by chemical probe-based array, *Nat Protoc* 20 (2025) 1057–1081.
- [63] J. Rezaie, M. Feghhi, T. Etemadi, A review on exosomes application in clinical trials: perspective, questions, and challenges, *Cell Commun. Signal.* 20 (1) (2022) 145.
- [64] A. Liu, G. Yang, Y. Liu, T. Liu, Research progress in membrane fusion-based hybrid exosomes for drug delivery systems, *Front. Bioeng. Biotechnol.* 10 (2022) 939441.
- [65] L. Cheng, X. Zhang, J. Tang, Q. Lv, J. Liu, Gene-engineered exosomes-thermosensitive liposomes hybrid nanovesicles by the blockade of CD47 signal for combined photothermal therapy and cancer immunotherapy, *Biomaterials* 275 (2021) 120964.
- [66] M. Piffoux, A.K.A. Silva, C. Wilhelm, F. Gazeau, D. Tareste, Modification of extracellular vesicles by fusion with liposomes for the design of personalized biogenic drug delivery systems, *ACS Nano* 12 (7) (2018) 6830–6842.
- [67] J. Mondal, S. Pillarisetti, V. Junnuthula, M. Saha, S.R. Hwang, I.K. Park, Y.K. Lee, Hybrid exosomes, exosome-like nanovesicles and engineered exosomes for therapeutic applications, *J. Contr. Release* 353 (2023) 1127–1149.
- [68] N.A. Hodges, E.M. Sussman, J.P. Stegemann, Aseptic and septic prosthetic joint loosening: impact of biomaterial wear on immune cell function, inflammation, and infection, *Biomaterials* 278 (2021) 121127.